

NASA TECHNICAL NOTE



NASA TN D-2786

2.1

LOAN COPY: REFUR  
AFWL (WLIL-2)  
KIRTLAND AFB, N M

0079647



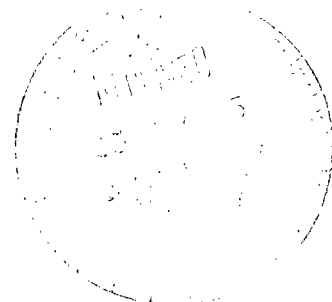
TECH LIBRARY KAFB, NM

NASA TN D-2786

# AERODYNAMIC CHARACTERISTICS OF TWO TRAILBLAZER II BLUNTED $9^\circ$ CONE REENTRY BODIES AT MACH 6.8 IN AIR AND 21.2 IN HELIUM

*by Herbert R. Schippell, Luther Neal, Jr.,  
and Don C. Marcum, Jr.*

*Langley Research Center  
Langley Station, Hampton, Va.*





**AERODYNAMIC CHARACTERISTICS OF TWO TRAILBLAZER II  
BLUNTED  $9^{\circ}$  CONE REENTRY BODIES AT MACH 6.8**

**IN AIR AND 21.2 IN HELIUM**

**By Herbert R. Schippell, Luther Neal, Jr.,  
and Don C. Marcum, Jr.**

**Langley Research Center  
Langley Station, Hampton, Va.**

**NATIONAL AERONAUTICS AND SPACE ADMINISTRATION**

---

**For sale by the Clearinghouse for Federal Scientific and Technical Information  
Springfield, Virginia 22151 - Price \$2.00**



# AERODYNAMIC CHARACTERISTICS OF TWO TRAILBLAZER II

## BLUNTED $9^\circ$ CONE REENTRY BODIES AT MACH 6.8

### IN AIR AND 21.2 IN HELIUM

By Herbert R. Schippell, Luther Neal, Jr.,  
and Don C. Marcum, Jr.  
Langley Research Center

#### SUMMARY

The normal-force, axial-force, and pitching-moment coefficients of scale models of two  $9^\circ$ -blunted-cone reentry bodies with their afterbodies have been measured in wind-tunnel tests. The bluntest of these is a scale model of the reentry body used on Trailblazer IIa. The other is a similar model of a proposed Trailblazer II reentry body with decreased nose bluntness. Tests were conducted in air at angles of attack from  $0^\circ$  to  $180^\circ$  at a Mach number of 6.8 and a Reynolds number per foot of  $1.68 \times 10^6$ . Tests were also conducted in helium at angles of attack from  $0^\circ$  to  $56^\circ$  at a Mach number of 21.2 and a Reynolds number per foot of  $8.64 \times 10^6$ . The experimentally measured coefficients are compared with values predicted by a modified Newtonian theory and result in generally good agreement throughout the angle-of-attack range. The angle of attack at which afterbody effects begin to become measurable corresponds to that predicted by Newtonian theory. A six-degree-of-freedom motion study to estimate the reentry-body motions indicates that the angle of attack converges and does not exceed the physical boundary angle ( $19.8^\circ$ ) of the bodies with nozzle and antenna afterbody components.

#### INTRODUCTION

The reentry of various objects into the earth's atmosphere at meteoric and intercontinental ballistic missile velocities creates many problems in the fields of aerodynamics and physics. These problems stem from lack of theoretical knowledge or experimental measurement of the exact properties of the hot gas between the shock front and the body surface. However, some phenomena are known to occur and can be measured; for example, light is emitted at many wavelengths and the analysis of this light provides useful high-temperature air data. The reflection of a radar wave from a reentry object immersed within the ionized gas wake contains information about the electromagnetic properties of high-temperature air.

In order systematically to vary the amount of ionized gas and its luminosity, two reentry bodies each with a different nose bluntness have been prepared for comparative flights on the Trailblazer II vehicle. The Trailblazer II rocket vehicle is an inexpensive solid-propellant rocket vehicle and is capable of delivering a 40-pound payload downward into the earth's atmosphere at about 20 000 feet per second. Reported in reference 1 is a description and evaluation of the performance of three Trailblazer II rocket vehicles - IIa, IIb, and IIc.

The effect of the aerodynamic characteristic of nose bluntness on the electromagnetic and luminous efficiency may be obtained by comparing the in-flight radar and optical data obtained on the two reentry bodies of the present investigation. The two comparative reentry bodies being studied are  $9^\circ$  blunted cones with the same base diameter but different bluntness ratios (ratio of nose radius to base radius). The bluntest model is a model of the reentry body flown on the Trailblazer IIa vehicle. In order to allow communications from the reentry body, a rear-mounted antenna in the shape of a flared skirt was incorporated into the design. This flared-skirt afterbody served two purposes on the reentry body. It served as a telemeter antenna and as a highly polished mirror for reflecting light from a light source onboard the reentry body.

The purpose of this paper is to present the results of wind-tunnel force and moment tests conducted on scale models of the two comparative reentry bodies and their various afterbodies. The investigation was conducted at a Mach number of 6.8 in air and a Mach number of 21.2 in helium. The angle of attack was varied from  $0^\circ$  to  $180^\circ$  in air and from  $0^\circ$  to  $56^\circ$  in helium. The pertinent Newtonian theory, with a modification, and the results of a limited analytical study of the dynamical motions are presented. Schlieren photographs are presented for representative angles of attack which should aid in defining the flow field about the body.

## SYMBOLS

A body-axis system is used as the reference frame for the forces and moments presented herein. The moment center is also the center-of-gravity location shown on figures 1 and 2, respectively. Bluntness ratio is defined as the ratio of nose radius to base radius.

A	base area of body alone, sq ft
$C_A$	axial-force coefficient, $\frac{\text{Total axial force}}{q_\infty A}$
$C_D$	drag coefficient, $\frac{\text{Drag}}{q_\infty A}$
$C_m$	pitching-moment coefficient, $\frac{\text{Pitching moment}}{q_\infty A d}$

$C_{mq}$	pitch damping derivative, $\frac{\partial(C_m)}{\partial\left(\frac{qd}{2V}\right)}$ , per radian
$C_N$	normal-force coefficient, $\frac{\text{Normal force}}{q_\infty A}$
$d$	base diameter of body alone, ft
$M$	Mach number
$q$	body pitching velocity, radians per second
$q_\infty$	dynamic pressure, lb/sq ft
$R$	Reynolds number per foot
$V$	velocity, fps
$W$	weight, lb
$x_{cp}$	distance to center of pressure from nose, fraction of base diameter
$\alpha$	angle of attack, deg
$\beta$	angle of sideslip, deg
$\eta$	total yaw angle, $\sqrt{\alpha^2 + \beta^2}$
$\gamma$	flight-path angle measured from local vertical, radians
Subscripts:	
max	maximum
min	minimum

## APPARATUS AND TESTS

Two wind tunnels, the Langley 11-inch hypersonic tunnel (with air as the test medium) and the Langley 22-inch helium tunnel, were utilized to accomplish the testing. Both of these tunnels are of intermittent type and operate on the blowdown principle.

The forces and moments on the models were measured on six-component strain-gage balances and no corrections have been included in the data for the pressure acting inside the balance shield. The angle of attack of the model was varied from  $0^\circ$  to  $180^\circ$  in air and from  $0^\circ$  to  $56^\circ$  in helium. Models with three

different sting-mount-hole locations were necessary in the air tests in order to cover the large angle-of-attack range. Only rear sting-mounted models were used in the helium tests. Angle-of-attack measurements were made optically by reflecting a point source of light on a calibrated scale. This optical technique gives the true geometric angle of attack of the body irrespective of the deflection of the balance and sting under load. Angles of attack are estimated to be accurate within  $\pm 0.2^\circ$ .

#### Air Tests at $M = 6.8$

The tests in air were conducted in the Langley 11-inch hypersonic tunnel which utilizes different fixed-geometry nozzles to facilitate testing at different Mach numbers. A typical calibration of the nozzle in which the present tests were conducted is the principal nozzle in reference 2 and a description of the remainder of the facility is presented in reference 3.

The average test conditions included a Mach number of 6.8, a stagnation pressure of 10 atmospheres, and a stagnation temperature of  $550^\circ\text{F}$ . This level of stagnation temperature was sufficient to prevent the liquefaction of air in the test section. The Reynolds number per foot corresponding to these test conditions is about  $1.68 \times 10^6$ . The Mach number has an accuracy of about  $\pm 0.05$ . The full-scale flight Reynolds number per foot that corresponds to this Mach number is  $4.75 \times 10^6$ .

#### Helium Tests at $M = 21.2$

The high Mach number tests were conducted in the Langley 22-inch helium tunnel. This tunnel also utilizes different fixed-geometry nozzles to facilitate testing at different Mach numbers, and for these tests a contoured nozzle was used. Further details concerning this tunnel are given in reference 4.

The average test conditions in helium included a Mach number of 21.2, a stagnation pressure of 137 atmospheres, and a stagnation temperature of  $70^\circ\text{F}$ . The Reynolds number per foot based on these test conditions is about  $8.64 \times 10^6$ . The Mach number has an accuracy of about  $\pm 0.2$ . The full-scale flight Reynolds number per foot that corresponds to this test Mach number is  $1.79 \times 10^4$ . The wind-tunnel test Reynolds number per foot of  $8.6 \times 10^6$  corresponds to the full-scale flight conditions at  $M = 17.4$ .

#### Models

The aerodynamic characteristics of two  $9^\circ$  cone models of different nose-bluntness ratios with and without afterbodies are the test objectives, and sketches of these configurations are shown as figures 1 and 2. Figure 1 shows model 1 which has a bluntness ratio of 0.660. Model 1 is a scale model of the Trailblazer IIa reentry body. Figure 2 shows model 2 which has a bluntness ratio of 0.324. As mentioned previously, three separate models of each of the different nose-bluntness ratios were necessary for the tests in air in order to

cover the large angle-of-attack range. Also, the balance-load capability and the size of the uniform test core of the tunnel nozzle necessitated the use of models of different scale. Sketches of the three models showing the different sting-mounting hole locations are shown in parts (a), (b), and (c) of figures 1 and 2. Figures 1(a) and 2(a) show the 0.117-scale models which were sting mounted from the rear. These models were used to obtain the air data at angles of attack from  $0^\circ$  to  $27^\circ$  as well as the helium data at angles of attack from  $0^\circ$  to  $56^\circ$ . Figures 1(b) and 2(b) show side-mounted 0.102-scale models which were used to obtain air data for angles of attack from  $33^\circ$  to  $147^\circ$  for model 1 and from  $33^\circ$  to  $137^\circ$  for model 2. At higher angles of attack the data were obtained with the nose-mounted 0.102-scale models shown in figures 1(c) and 2(c). In addition, for model 1 only, the rear-sting-mounted 0.117-scale model (fig. 1(a)) was tested for  $30^\circ \leq \alpha < 60^\circ$ , and the test results when compared with those obtained with the side-mounted models showed no measurable effects due to the difference in sting-mounting methods for this angle-of-attack range.

Figure 3 illustrates the three configurations that were tested. Figure 3(a) shows the basic body alone (model 1); figure 3(b) shows the basic body plus a scale model of a rocket exhaust nozzle, and figure 3(c) shows the basic body plus a flared skirt-shaped antenna encircling the nozzle.

#### THEORETICAL METHODS

The theoretical aerodynamic forces and moments were computed for the body-alone models over the angle-of-attack range from  $0^\circ$  to  $180^\circ$  by using a combination of Newtonian and modified Newtonian theory over different portions of the body. An explanation concerning the use of the theory in this combination is contained in reference 5 and a brief description is written here. The Newtonian (or impact) expression for the local pressure coefficient was used in computing the force contributions of the cone frustums whereas the modified Newtonian pressure coefficient was used in computing the force contributions of the spherical segments and flat bases. The overall integrated coefficients were computed utilizing the equations and tables of reference 6. The results of the theoretical calculations are for a specific heat ratio of 1.4 and  $M = 6.8$  and are shown on all appropriate figures. The model base was assumed to be a flat circular disk with no holes in it.

The flow-turn angle at the base of the full-scale model 1 body-alone configuration has been theoretically estimated and is given in references 7 and 8. These references also contain results of the flow-field calculations that have been applied to the full-scale configuration of model 1 with no afterbody. Moreover, for flight conditions with an angle of attack of  $0^\circ$ , altitude of 100 000 feet, velocity of about 15 900 feet per second, and  $M = 16.0$ , the flow-turn angle as determined from the plots of reference 7 is  $13.50^\circ$  for equilibrium-flow conditions and  $9.0^\circ$  for frozen-flow conditions. The physical boundary, according to the dimensions of model 1 with the flared antenna afterbody, requires the flow to turn through an angle of about  $19.8^\circ$  before impingement would occur. Thus according to the theoretical estimates made at  $\alpha = 0^\circ$  the flow does not impinge on any of the afterbody components; instead, these components are immersed in the dead-air wake. However, since the effect of angle of attack on the flow-turning angle was not included in the theoretical study of references 7 and 8, the physical boundary angle  $19.82^\circ$  is taken as the allowable



angle through which the body can be pitched before any flow of higher dynamic pressures than the dead-air values would impact directly on the flared antenna of the afterbody. The adequacy of this assumption is borne out by the experimental data presented herein, and more discussion on this assumption is included in a subsequent section on pitching moment.

## RESULTS AND DISCUSSION

### General Remarks

The wind-tunnel tests were conducted in two different test mediums; air and helium. The air testing defined the aerodynamic forces and moments on all three afterbody variations of each model throughout the angle-of-attack range from  $0^\circ$  to  $180^\circ$ . Most of the basic body-alone data have been published previously (ref. 5) and is repeated here for comparison. Definition of the forces and moments at large angles of attack is necessary because interference effects between the body and afterbody cause the theory to have a questionable application. The chief aim of the helium experiment was to obtain some understanding of the angle of attack at which the large flared antenna-afterbody structure would experience aerodynamic forces at the higher Mach numbers. No attempt has been made to treat the subject of air-helium simulation in this paper. Much work has been done on this subject and some pertinent information on it may be found in references 9 to 13.

The schlieren photographs shown as figure 4 were obtained in air at the test conditions of  $M = 6.8$ ,  $R = 1.68 \times 10^6$ . The data contained in figures 5 to 8 were obtained at the test conditions of  $M = 6.8$  and  $R = 1.68 \times 10^6$  in air, and  $M = 21.2$  and  $R = 8.64 \times 10^6$  in helium.

### Flow-Field Characteristics

Figure 4 is composed of schlieren photographs that were taken during the air tests and are presented for angle-of-attack increments of about  $30^\circ$ . Schlieren photographs furnish a direct measurement of the shock-wave shape and standoff distance. They also illustrate interference effects and aid in identifying various elements of the flow field around the body and in the near wake.

A definition of the shock-wave shape that accompanies a reentry body is necessary before an understanding of the thermodynamic and fluid dynamics of the flow field that surrounds the body can be gained. These schlieren photographs may also indirectly aid in understanding the wake phenomena which are associated with a high-speed reentry body.

### Aerodynamic Coefficients

The experimental values of the aerodynamic coefficients  $C_N$ ,  $C_A$ , and  $C_m$  that were obtained in both air and helium are shown as a function of angle of attack in figures 5, 6, and 7, respectively. The coefficients have been

predicted by theory for the body-alone configuration of both models 1 and 2 in air, and these results are presented for comparison purposes on all the applicable figures. The ability of the theory to predict the experimental trends of both the forces and moments throughout the entire angle-of-attack range is, in general, good but fairly large deviations between the theory and experiment occur in several regions. Reference 5 contains an explanation of several of these deviations and includes some discussion of various nose-bluntness effects that are relevant to these bodies but are not treated in this paper.

Normal-force coefficient.- The variation of normal-force coefficient with angle of attack for both of the models and their various afterbody configurations is shown in figure 5. At  $\alpha = 0^\circ$  the slope of the normal-force curve is approximately 50 percent and 60 percent below that predicted by theory for models 1 and 2, respectively. As expected, skin friction is more important on the less blunt, or longer model, and the ability of impact-type theory to predict force and moment is slightly poorer. Also, as expected, the addition of afterbodies affects the normal force, but these effects are not significant up to angles of attack of about  $40^\circ$ . The afterbodies increase the value of the maximum normal force and cause it to occur at a higher angle of attack. For model 1, the addition of the largest afterbody increases the maximum value of  $C_N$  10 percent and changes the angle of attack at which it occurs from  $75^\circ$  to  $90^\circ$ . The addition of the same afterbody to model 2 changes the angle of attack at which maximum  $C_N$  occurs from  $80^\circ$  to  $85^\circ$  and increases the maximum value of  $C_N$  by about 6 percent. The helium data agree well with air data over the entire angle-of-attack range for model 2 and up to about  $30^\circ$  for model 1. At angles of attack above  $30^\circ$  and up to  $56^\circ$  the helium data are slightly higher than the air data for model 1.

Axial-force coefficient.- The variation of axial-force coefficient with angle of attack is shown in figure 6. The afterbodies show effectiveness at all angles of attack greater than  $70^\circ$ , and for angles of attack above  $150^\circ$  they act to produce a smaller absolute value of  $C_A$ . The air and helium data agree well over the entire angle-of-attack range of the tests with the exception of some slight variations. The data for model 1 show that the helium data are slightly lower than the air data at angles of attack near  $0^\circ$ . In the  $\alpha$  region between  $30^\circ$  and  $56^\circ$ , it is observed that the helium data show slightly larger values of axial-force coefficient than the air data for both models 1 and 2. The behavior of the axial-force coefficient is noteworthy in the region between  $\alpha = 150^\circ$  to  $\alpha = 180^\circ$  for both models. At  $\alpha = 180^\circ$  for model 1 and  $\alpha = 174^\circ$  for model 2, the body-alone configuration produces the largest absolute value of axial-force coefficient and the body with nozzle produces the smallest. The value for the body with nozzle and antenna falls in between the two. The schlieren photographs (fig. 4) provide some explanation of this behavior. The shock shapes at the base of the various afterbodies are noticeably different. These differences in shock shape correspond to those caused by a cone with varying degrees of nose bluntness. The bluntest cone would have the largest axial-force coefficient at  $\alpha = 0^\circ$  and the least blunt cone would have the smallest  $C_A$ , if nose bluntness were the only change involved. The body with nozzle shows the least blunt shock, the body-alone shows the bluntest shock, and the body with nozzle and antenna shows shock bluntness between these two. It follows, then, that the body with nozzle produces the smallest absolute value of axial-force coefficient and the flat-base body, the largest.

Pitching-moment coefficient.- The variation of pitching-moment coefficient with angle of attack is shown in figure 7 and illustrates the good general agreement between theory and experiment for the body alone. However, the theory does overestimate the negative slope of the pitching-moment curve near  $\alpha = 0^\circ$  for model 1. The pitch-up tendency of the basic body between  $\alpha = 60^\circ$  and  $\alpha = 90^\circ$  is not predicted and the second stable trim condition near  $\alpha = 180^\circ$  is also not predicted.

The angle of attack at which the difference in moment contribution of the various afterbodies becomes measurable is worthy of note. The afterbody with the large flared-skirt antenna is of particular concern because of its small aerodynamic-load-carrying capability on the full-scale reentry body. From the data shown in figure 7, the angle of attack at which this large flared-skirt antenna has been estimated to become effective is between  $15^\circ$  and  $20^\circ$  for air ( $M = 6.8$ ) and between  $17^\circ$  and  $22^\circ$  for helium ( $M = 21.2$ ). This is the angle of attack at which the aerodynamic loads on the afterbody surface produce a moment measurably different from that when the antenna flare is not present. Also, the allowable angle of attack of  $19.8^\circ$ , mentioned in the section "Theoretical Method" as the physical boundary angle, appears to fit these measured values and thus the assumption of using the physical boundary angle appears adequate.

As mentioned previously, there is a second stable trim condition near  $\alpha = 180^\circ$  for both model 1 and model 2. This condition is most pronounced for the body-nozzle configuration. The addition of the antenna flare to the nozzle reduces this effect to the minimum noted for the three configurations. Incidentally, this behavior corresponds to the elimination of this second stable trim point by the addition of sphere-cap afterbodies as discussed in reference 5. In reference 5 it was shown that these secondary stable trim conditions for the basic cones could be completely eliminated by adding spherical afterbody caps whose centers of curvature coincided with the respective moment centers.

Variation of  $C_m$  with  $C_N$ .- The stability parameter plots of  $C_m$  as a function of  $C_N$  are presented in figure 8 for both of the models and their various afterbody configurations. Although the testing was conducted throughout the entire angle-of-attack range, only the stability about the  $\alpha = 0^\circ$  trim point is illustrated. Both the air and helium data are presented and good agreement between the two is noted. Also, shown on all plots are the theoretical predictions for the body-alone configurations. The theory was computed for the conditions of  $M = 6.8$  and specific heat ratio of 1.4. It is observed from the figure that the theoretical curve for the body-alone model compares favorably with the measured data for the models with their afterbodies.

### Dynamic Analysis

The experimental data of figure 8 indicate only a small amount of static stability for model 1; consequently, the wind-tunnel results have been utilized in a dynamic analysis programed on an automatic computer to determine the contribution of the pitch damping coefficient of the reentry body in free flight just prior to reentry. The appropriate quantities used in the computer program

are given in table I. Quantities required for the computer study but not listed in table I were assumed to be zero. The ARDC Standard Atmosphere (ref. 14) was used.

A schematic drawing is shown in figure 9 to represent the orientation of the reentry body and the precession cone thought to be applicable near an altitude of 240 000 feet during the reentry phase of the flight. The reentry body is placed into this position in space by the Trailblazer II vehicle. Because of the spin stabilizing method used, the reentry body will probably be precessing as well as spinning just prior to its reentry.

Figure 10 contains the aerodynamic characteristics that were used in the computer program. These curves are approximations of the experimental data by a series of straight line segments. The approximations shown are for the body with nozzle and antenna afterbody in the case of model 1 and for the body with nozzle afterbody in the case of model 2. The change in center of pressure with Mach number for model 1 was estimated by using the method of reference 15. Reference 16 contains the method of trajectory analysis that is applicable to this study.

Figure 11 shows the results of the computer program. It is a plot showing the variation of total yaw angle, which is the effective angle of attack, and dynamic pressure with altitude. This analysis shows that the total yaw angle decreases with decreasing altitude and that the nozzle antenna afterbody will not become exposed to the airstream during reentry. The data in the figure are based on the value of pitch damping derivatives shown in table I. Values of aerodynamic damping were used in the computer but were not obtained in the wind-tunnel tests. Damping was used because it provided a more realistic estimate of the body motion. The values of the damping derivatives were estimated with the aid of the data contained in reference 17. However, a trajectory was computed with no damping and the envelope of the total yaw angle tended to converge with the same trend as that shown, but the convergence is less. The same necking down of the envelope at maximum dynamic pressure occurred in all cases. The curve for model 1 converges to a value of  $0.8^\circ$  at 80 000 feet altitude and the case wherein zero damping was considered converged in the same manner to a value of  $2.75^\circ$  at 80 000 feet altitude. The minimum side of the curve was the same in both cases. Since convergence was obtained for zero damping coefficient the amount of static stability present was considered sufficient. The envelope for body 1 converges differently from that for body 2 and since the ballistics coefficient ( $W/C_D A$ ), static margin, and pitch damping are different for each reentry body, it is difficult to pinpoint the exact reason for the difference.

#### CONCLUDING REMARKS

An analysis has been made of the experimental wind-tunnel data obtained at a Mach number of 6.8 and a Reynolds number per foot of  $1.68 \times 10^6$  in air and at a Mach number of 21.2 and a Reynolds number per foot of  $8.64 \times 10^6$  in helium on scale models of two reentry bodies of different nose bluntness ratios and with nozzle and flared antenna as afterbody components. The results indicate that

the angle of attack at which the large antenna flare afterbody causes significant aerodynamic effects is between  $15^{\circ}$  and  $20^{\circ}$  for a Mach number of 6.8 in air and between  $17^{\circ}$  and  $22^{\circ}$  for a Mach number of 21.2 in helium as determined experimentally, and these values are comparable to the angle  $19.8^{\circ}$  which is the physical boundary angle of the models. In general, modified Newtonian theory agrees with the data obtained. There is a second stable trim condition near  $180^{\circ}$  angle of attack for both models 1 and 2. This condition is most pronounced for the body-nozzle configuration, and the addition of the antenna flare to the nozzle reduces this effect to the minimum for the three configurations tested.

A six-degree-of-freedom motion study conducted to estimate the reentry body motions by using these wind-tunnel results indicates that the angle of attack converges and does not exceed the physical boundary angle ( $19.8^{\circ}$ ) of the bodies with afterbody components.

Langley Research Center,  
National Aeronautics and Space Administration,  
Langley Station, Hampton, Va., January 21, 1965.

## REFERENCES

1. Lundstrom, Reginald R.; Henning, Allen B.; and Hook, W. Ray: Description and Performance of Three Trailblazer II Reentry Research Vehicles. NASA TN D-1866, 1964.
2. Bertram, Mitchel H.: Exploratory Investigation of Boundary-Layer Transition on a Hollow Cylinder at a Mach Number of 6.9. NACA Rept. 1313, 1957. (Supersedes NACA TN 3546.)
3. McLellan, Charles H.; Williams, Thomas W.; and Beckwith, Ivan E.: Investigation of the Flow Through a Single-Stage Two-Dimensional Nozzle in the Langley 11-Inch Hypersonic Tunnel. NACA TN 2223, 1950.
4. Johnston, Patrick J.; and Snyder, Curtis D.: Static Longitudinal Stability and Performance of Several Ballistic Spacecraft Configurations in Helium at a Mach Number of 24.5. NASA TN D-1379, 1962.
5. Neal, Luther, Jr.: Aerodynamic Characteristics at a Mach Number of 6.77 of a  $9^\circ$  Cone Configuration, With and Without Spherical Afterbodies, at Angles of Attack up to  $180^\circ$  With Various Degrees of Nose Blunting. NASA TN D-1606, 1963.
6. Wells, William R.; and Armstrong, William O.: Tables of Aerodynamic Coefficients Obtained From Developed Newtonian Expressions for Complete and Partial Conic and Spheric Bodies at Combined Angles of Attack and Sideslip With Some Comparisons With Hypersonic Experimental Data. NASA TR R-127, 1962.
7. Kennedy, E.; Fields, A.; and Seidman, M.: The Calculation of the Flow Field About a Blunted  $9^\circ$  Cone - Section I. Tech. Rept. No. 256 (Contract AF 19 (604)-7400), Gen. Appl. Sci. Lab., Inc., Nov. 6, 1961. (Reissued Sept. 18, 1962.)
8. Bloom, M. H.; and Kennedy, E. D.: The Calculations of the Flow Field About a Blunted  $9^\circ$  Cone - Section II. Tech. Rept. No. 256 (Contract AF 19 (604)-7400), Gen. Appl. Sci. Lab., Inc., Jan. 2, 1962. (Reissued Sept. 18, 1962.)
9. Henderson, Arthur, Jr.: Recent Investigations of the Aerodynamic Characteristics of General and Specific Lifting and Nonlifting Configurations at Mach 24 in Helium, Including Air-Helium Simulation Studies. The High Temperature Aspects of Hypersonic Flow, Wilbur C. Nelson, ed., AGARDograph 68, Pergamon Press, 1964, pp. 163-190.
10. Love, Eugene S.; Henderson, Arthur, Jr.; and Bertram, Mitchel H.: Some Aspects of Air-Helium Simulation and Hypersonic Approximations. NASA TN D-49, 1959.

11. Arrington, James P.; and Maddalon, Dal V.: Aerodynamic Characteristics of Several Lifting and Nonlifting Configurations at Hypersonic Speeds in Air and Helium. NASA TM X-918, 1964.
12. Ladson, Charles L.: A Comparison of Aerodynamic Data Obtained in Air and Helium in the Langley 11-Inch Hypersonic Tunnel. NASA TM X-666, 1962.
13. Ladson, Charles L.; and Blackstock, Thomas A.: Air-Helium Simulation of the Aerodynamic Force Coefficients of Cones at Hypersonic Speeds. NASA TN D-1473, 1962.
14. Minzner, R. A.; Champion, K. S. W.; and Pond, H. L.: The ARDC Model Atmosphere, 1959. Air Force Surv. in Geophys. No. 115 (AFCRC-TR-59-267), Air Force Cambridge Res. Center, Aug. 1959.
15. Briggs, J. L.: Correlation of Sphere Cone Center of Pressure and Normal Force Coefficient Slope. Aerodyn. Data Memo No. 1:76, Missile and Space Vehicle Dept., Gen. Elec. Co., June 4, 1962.
16. James, Robert L., Jr. (With Appendix B by Norman L. Crabill): A Three-Dimensional Trajectory Simulation Using Six Degrees of Freedom With Arbitrary Wind. NASA TN D-641, 1961.
17. Fisher, Lewis R.: Equations and Charts for Determining the Hypersonic Stability Derivatives of Combinations of Cone Frustums Computed by Newtonian Impact Theory. NASA TN D-149, 1959.

TABLE I.- COMPUTER INPUT DATA

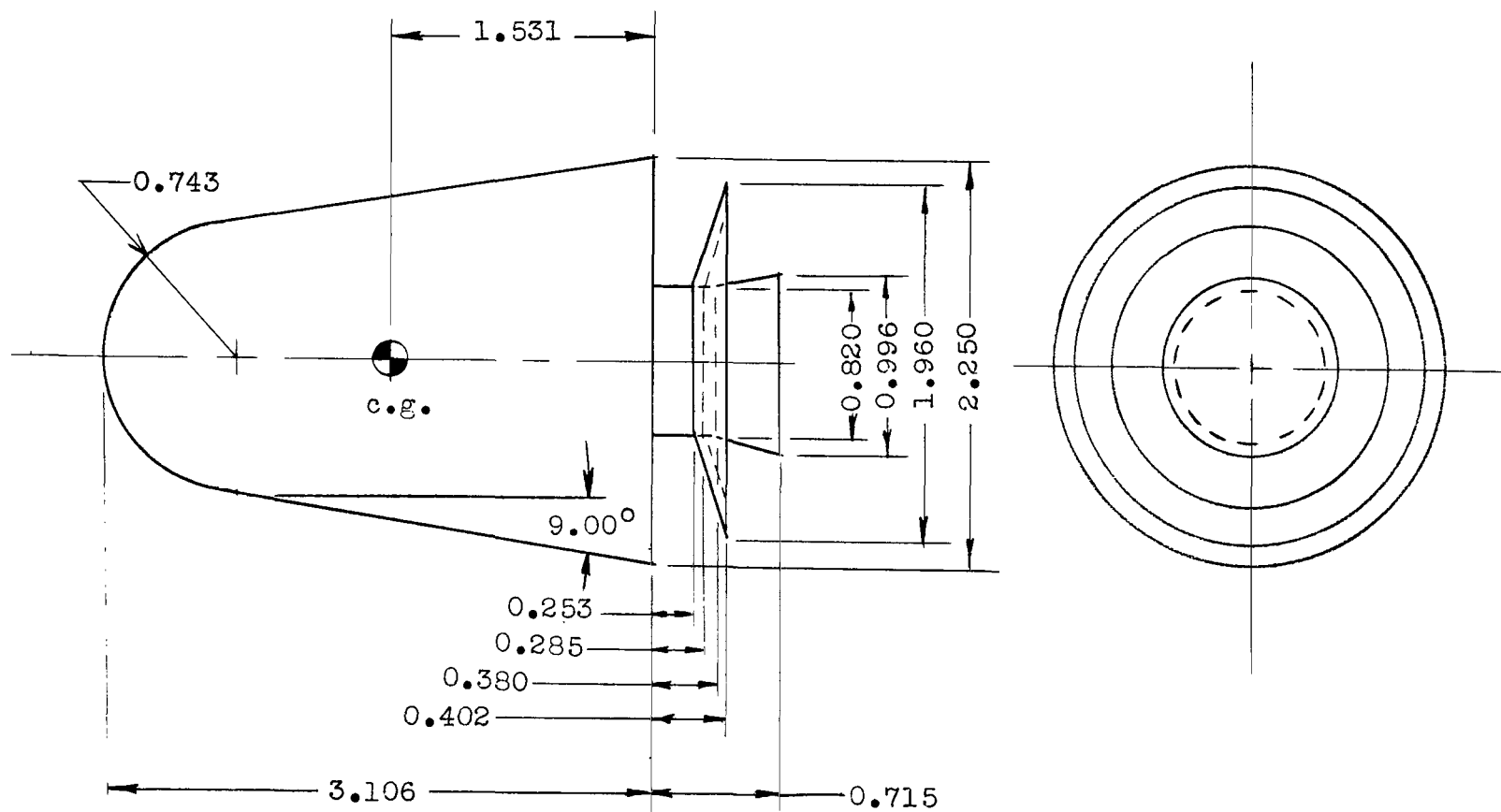
## Model 1, body with nozzle and antenna:

Center-of-gravity location, body diameters aft of nose . . . . .	0.662
Weight, lb . . . . .	41.12
Roll inertia, slug-ft <sup>2</sup> . . . . .	0.215
Pitch and yaw inertia, slug-ft <sup>2</sup> . . . . .	0.863
Gravity, ft/sec <sup>2</sup> . . . . .	31.60
Reference area, ft <sup>2</sup> . . . . .	2.0
Reference length, ft . . . . .	1.0
Longitudinal velocity component, fps . . . . .	20 285.0
Velocity component in yaw plane, fps . . . . .	0
Velocity component in pitch plane, fps . . . . .	5435.0
Horizontal range, ft . . . . .	0
Altitude, ft . . . . .	250 000
Flight-path angle, radians . . . . .	0.461
Roll rate, radians/sec . . . . .	-87.4
Yawing velocity, radians/sec . . . . .	-1.90
Pitch damping derivative, $C_{mq}$ , per radian, arbitrarily chosen to be constant . . . . .	-3.148

## Model 2, body with nozzle:

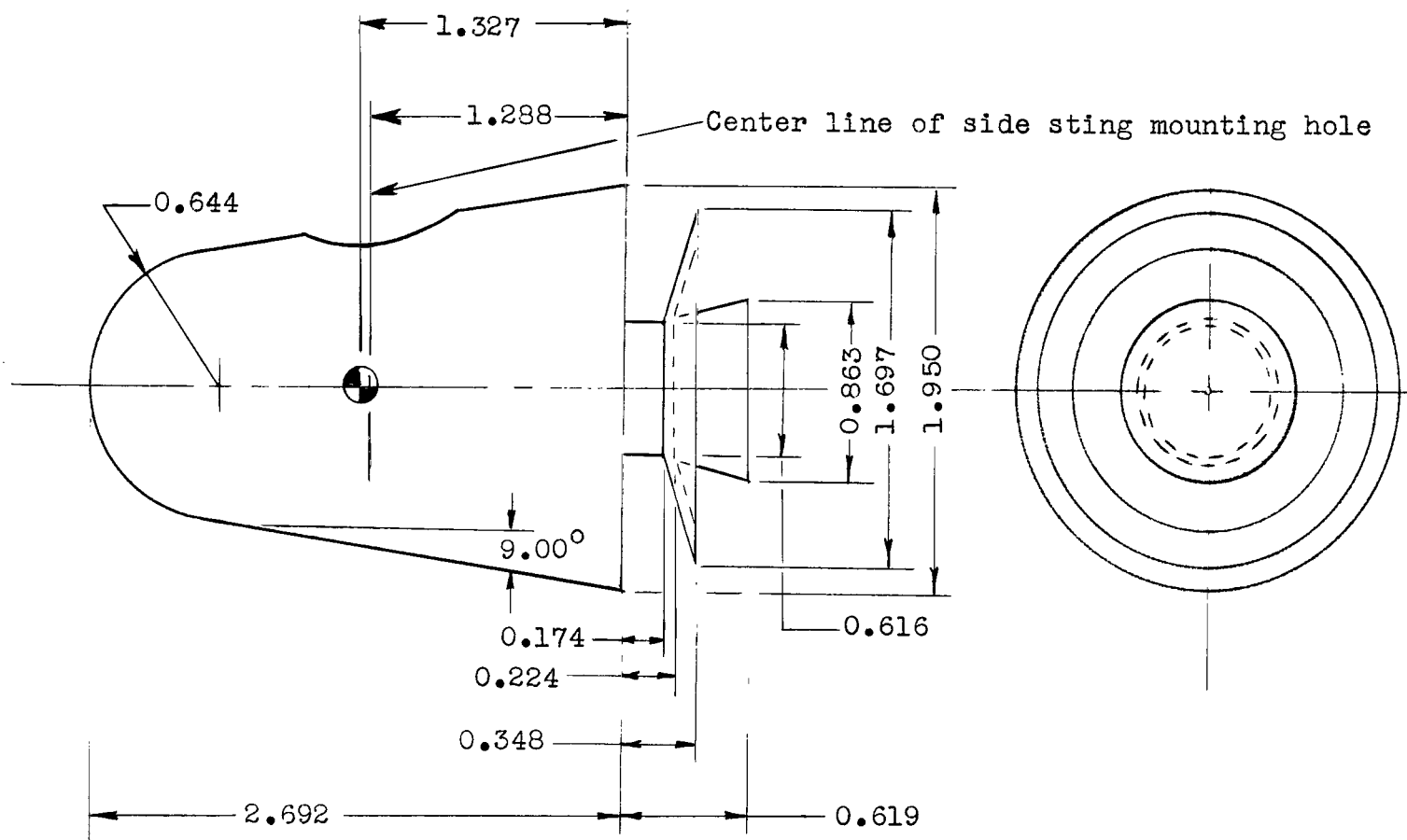
Center-of-gravity location, body diameters aft of nose . . . . .	1.252
Weight, lb . . . . .	30.38
Roll inertia, slug-ft <sup>2</sup> . . . . .	0.196
Pitch and yaw inertia, slug-ft <sup>2</sup> . . . . .	2.317
Gravity, ft/sec <sup>2</sup> . . . . .	31.869
Reference area, ft <sup>2</sup> . . . . .	2.0
Reference length, ft . . . . .	1.0
Longitudinal velocity component, fps . . . . .	20 285.0
Velocity component in yaw plane, fps . . . . .	0
Velocity component in pitch plane, fps . . . . .	5435.0
Horizontal range, ft . . . . .	0
Altitude, ft . . . . .	250 000
Flight-path angle, radians . . . . .	0.461
Roll rate, radians/sec . . . . .	-87.4
Yawing velocity, radians/sec . . . . .	-0.645
Pitch damping derivative, $C_{mq}$ , per radian, arbitrarily chosen to be constant . . . . .	-4.086





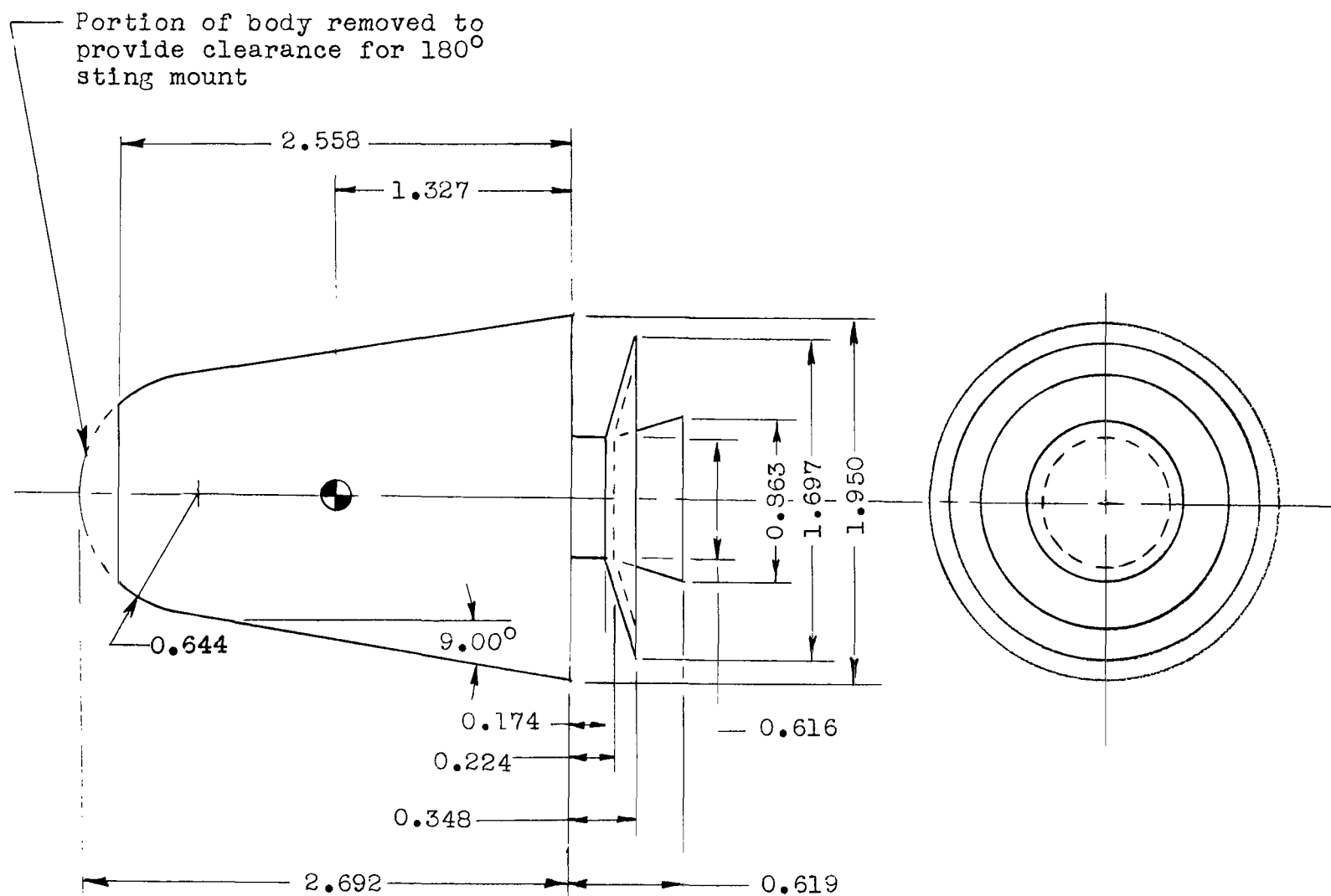
(a) Sting mounted from the rear.

Figure 1.- Sketch of model 1 showing the principal dimensions.  
All dimensions are in inches.



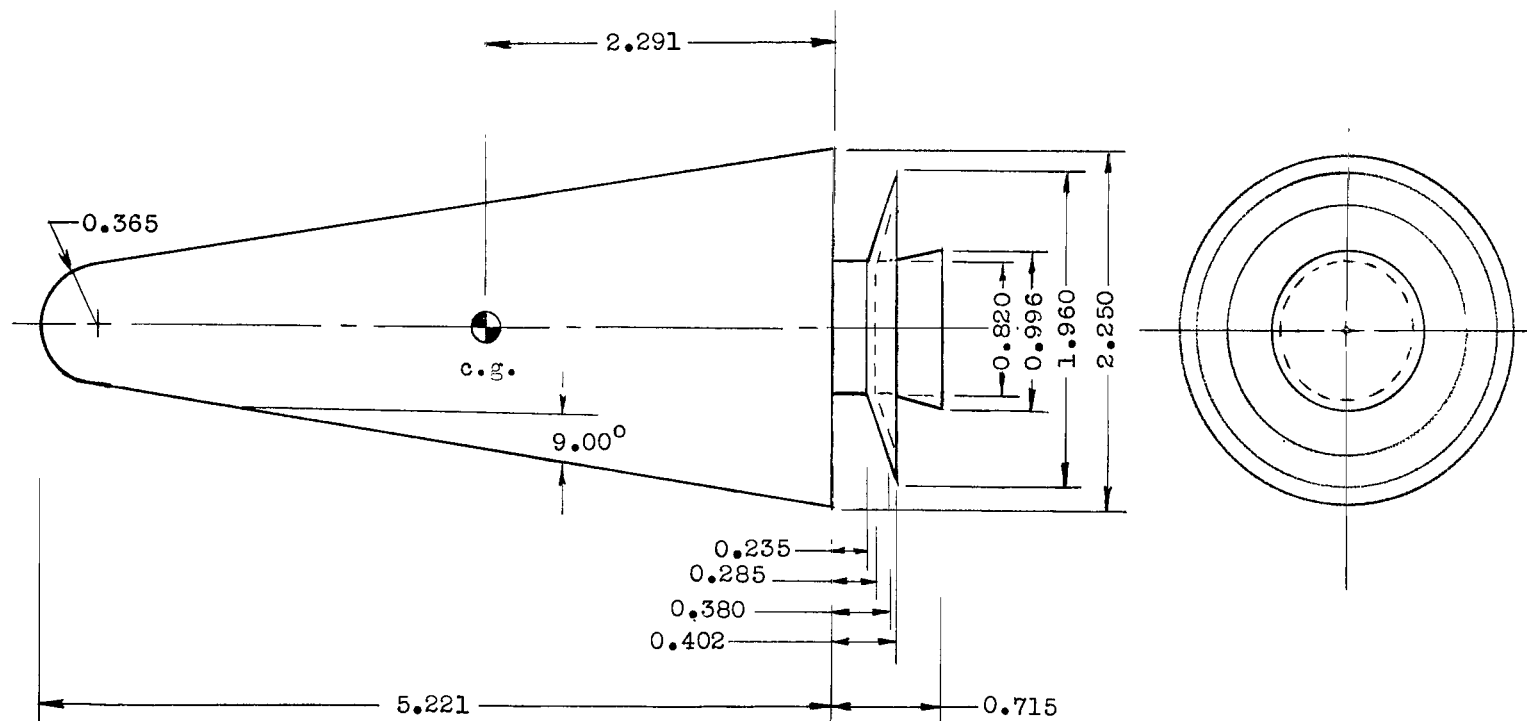
(b) Sting mounted from the side.

Figure 1.- Continued.



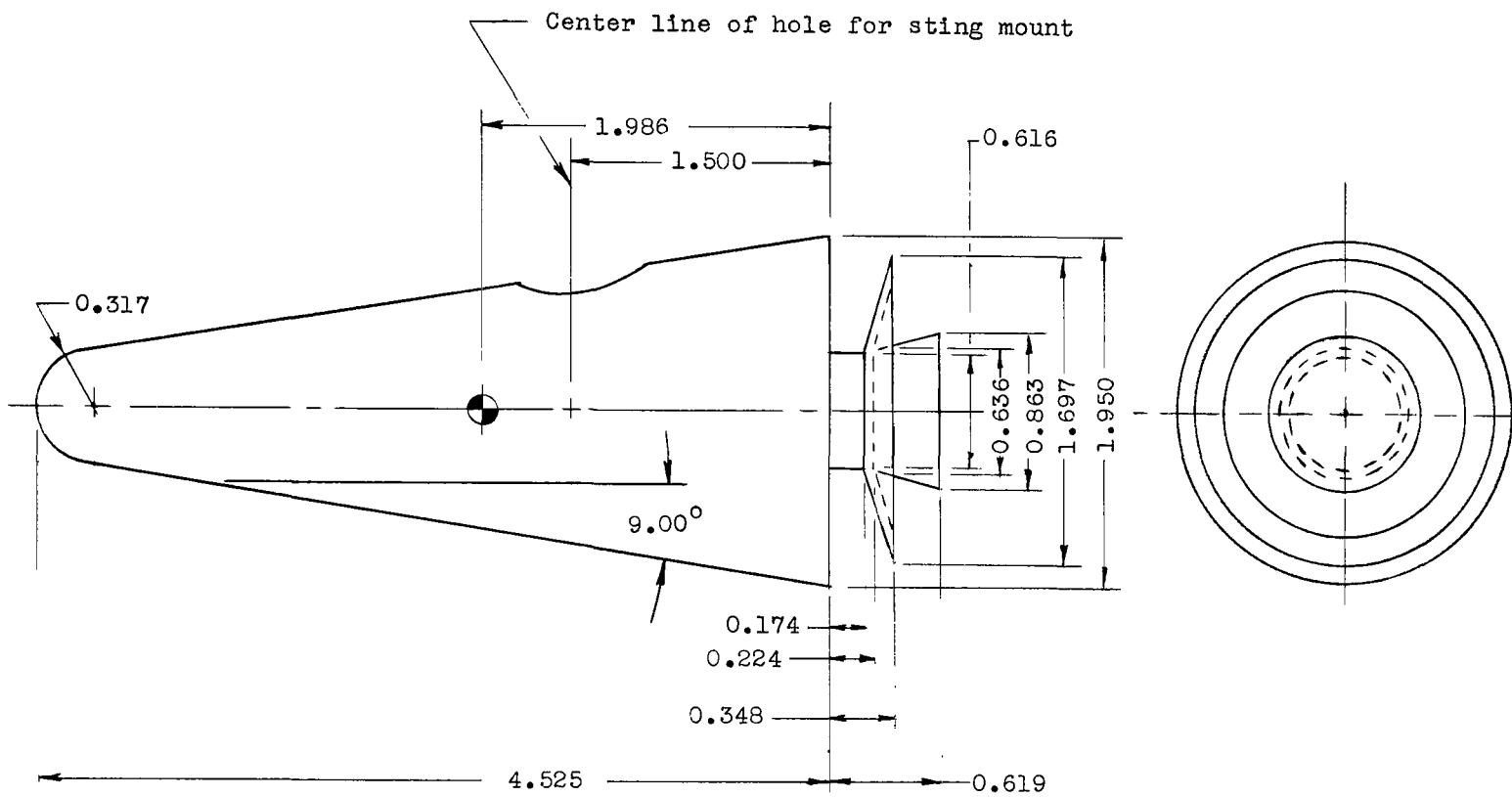
(c) Sting mounted from the nose.

Figure 1.- Concluded.



(a) Sting mounted from the rear.

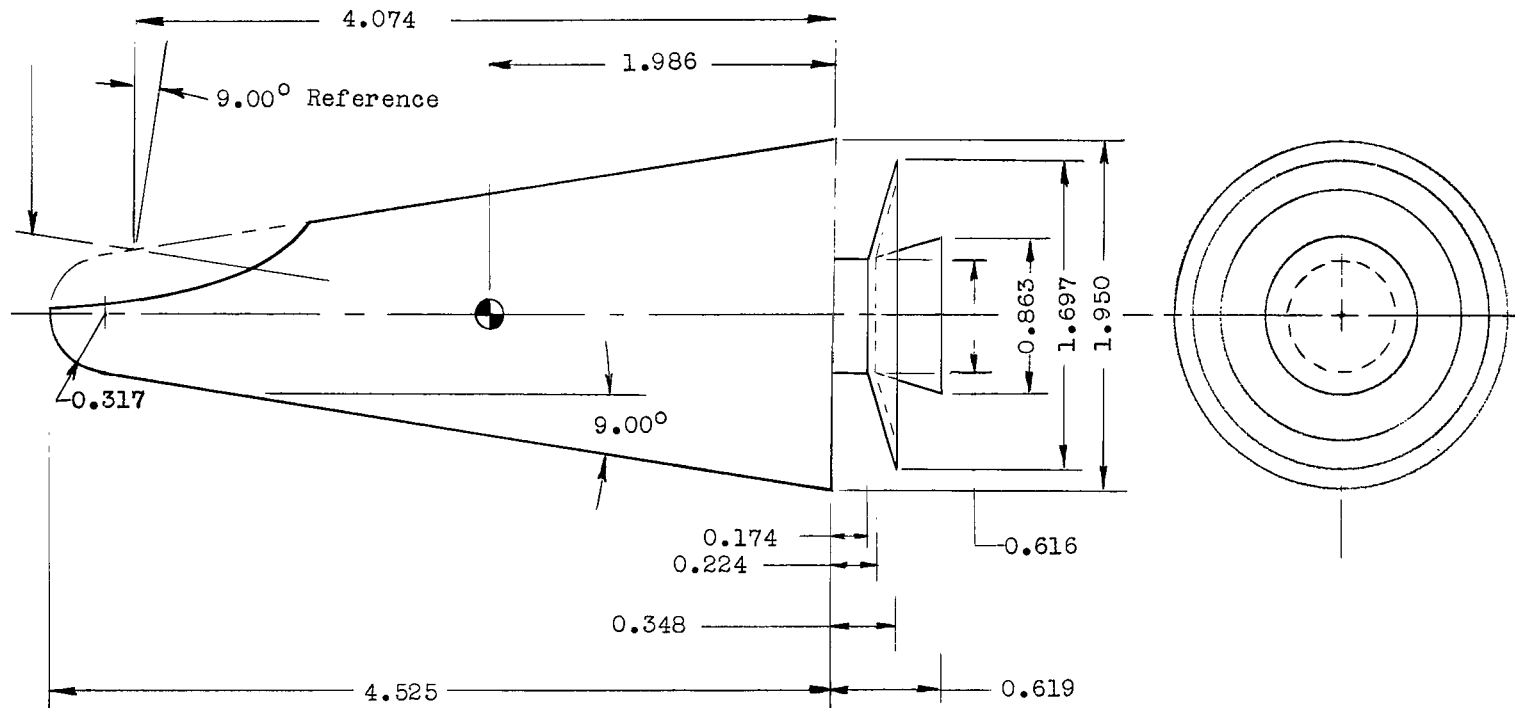
Figure 2.-Sketch of model 2 showing the principal dimensions.  
All dimensions are in inches.



(b) Sting mounted from the side.

Figure 2.- Continued.

— Center line of sting mount hole

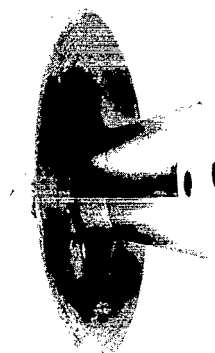


(c) Sting mounted 9° off center line of nose.

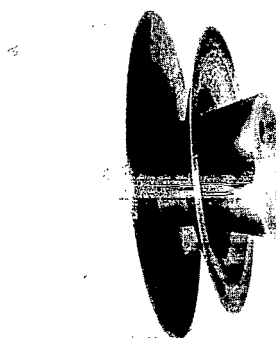
Figure 2.- Concluded.



(a) Body alone.



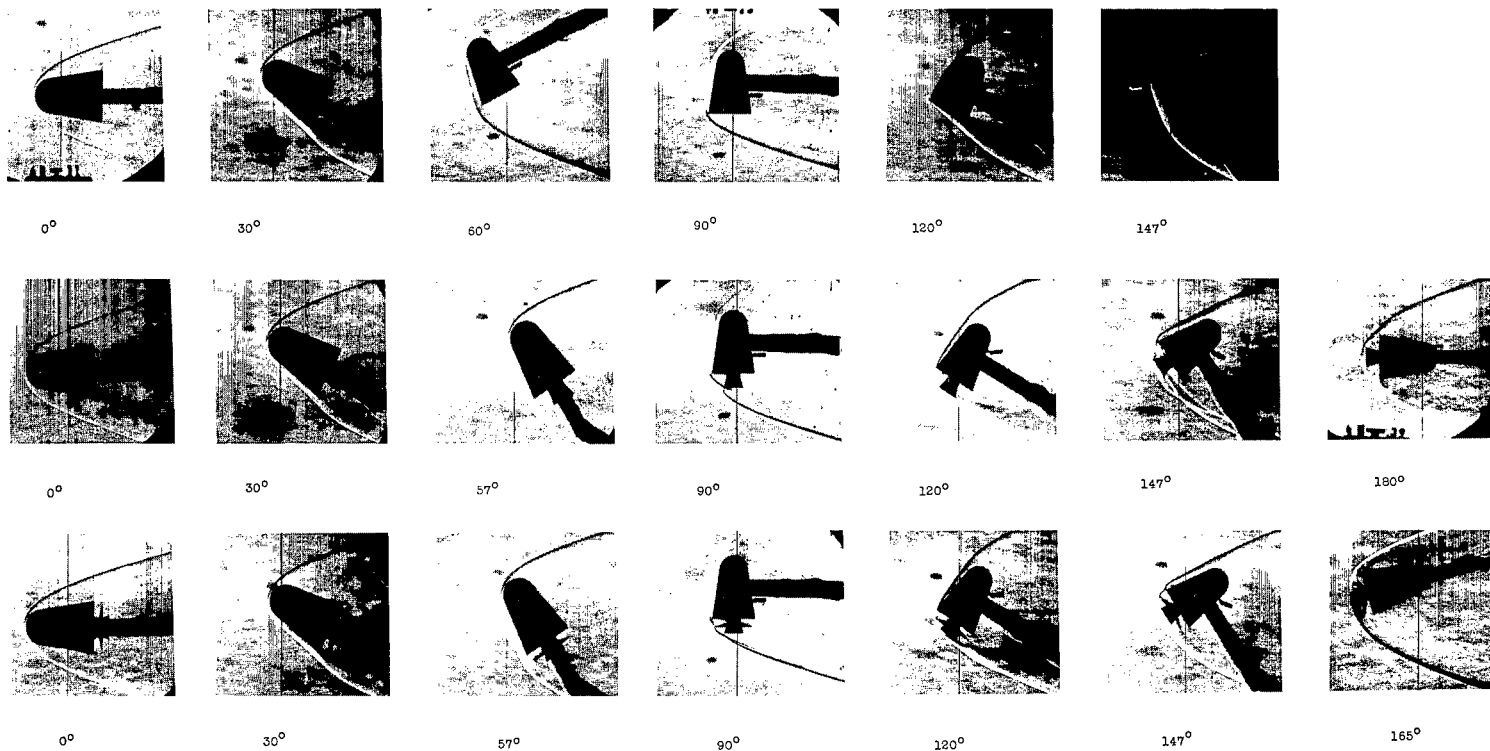
(b) Body with nozzle only.



(c) Body with nozzle and antenna.

L-65-15

Figure 3.- Photographs of model 1 illustrating afterbody variations.

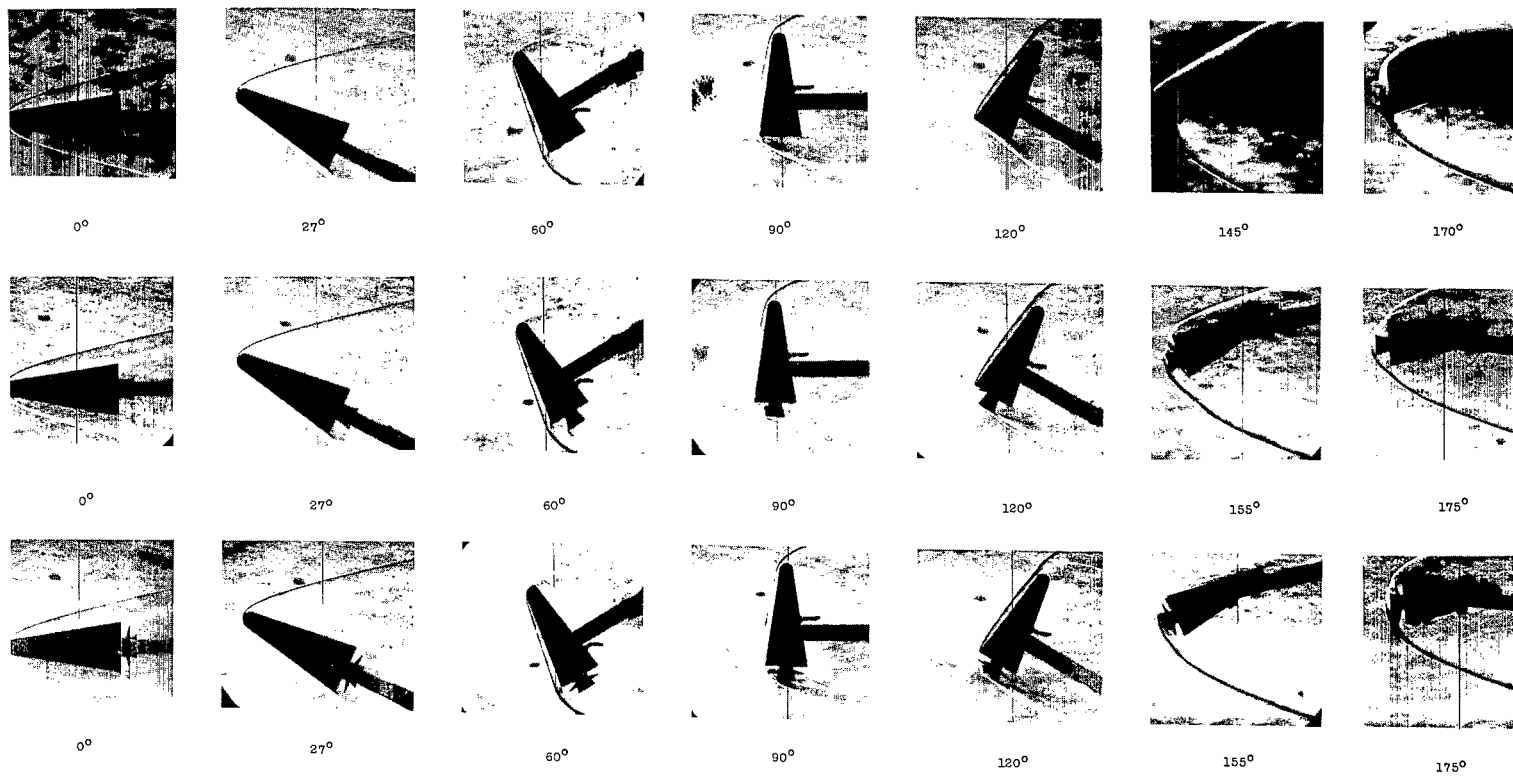


(a) Model 1.

L-65-13

Figure 4.- Schlieren photographs of models with and without nozzle and antenna at various angles of attack.

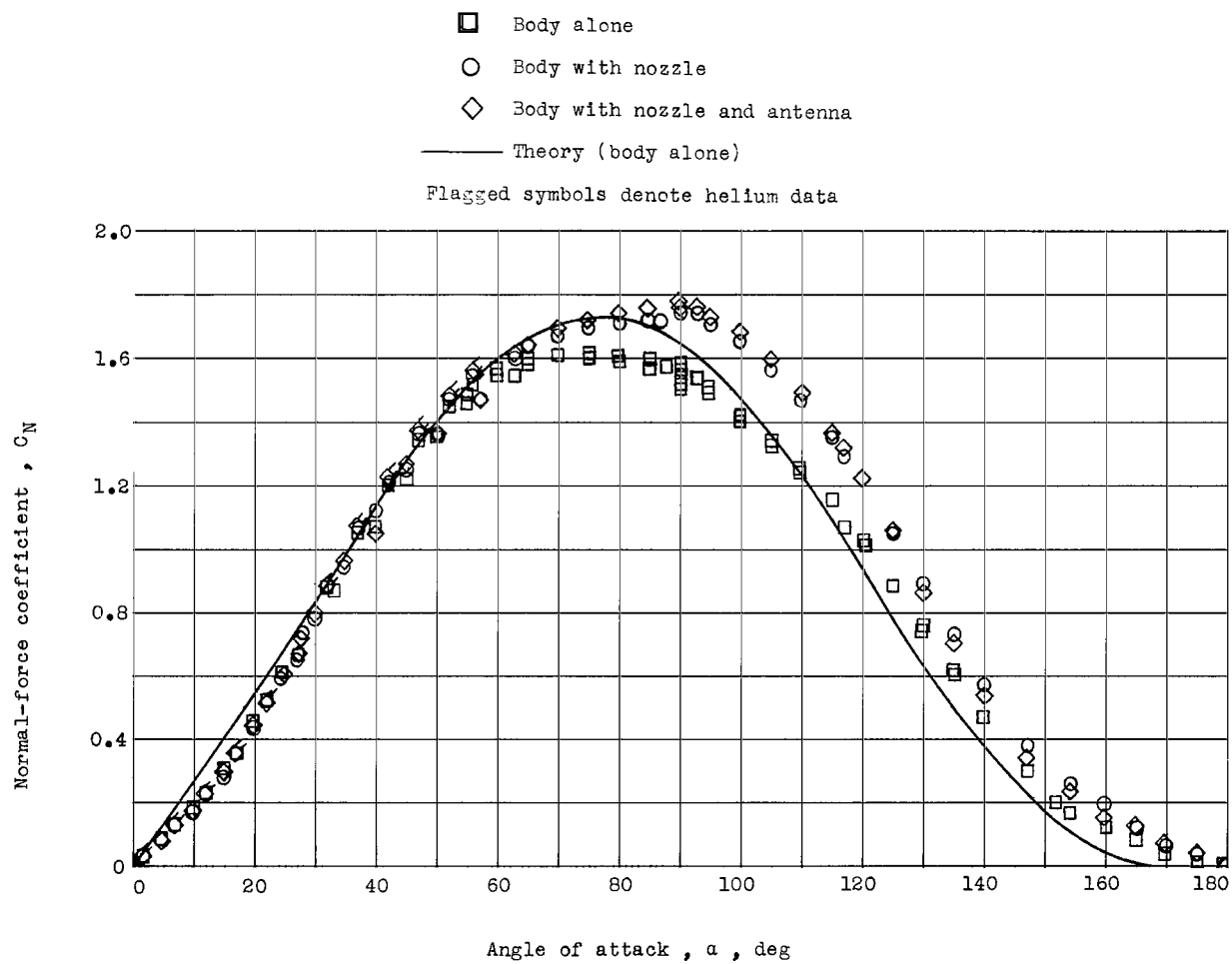




(b) Model 2.

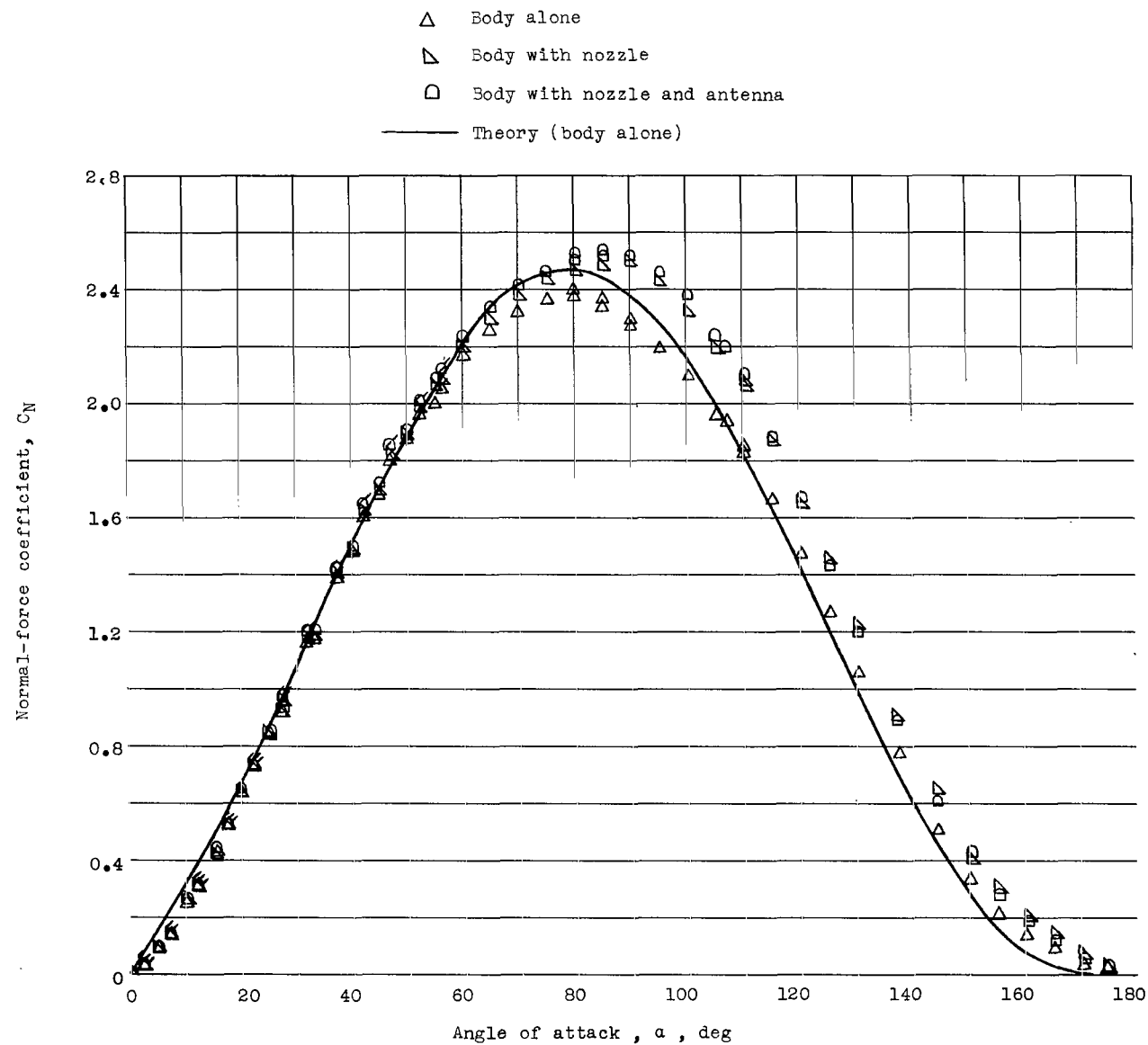
L-65-14

Figure 4.- Concluded.



(a) Model 1.

Figure 5.- Variation of normal-force coefficient with angle of attack.

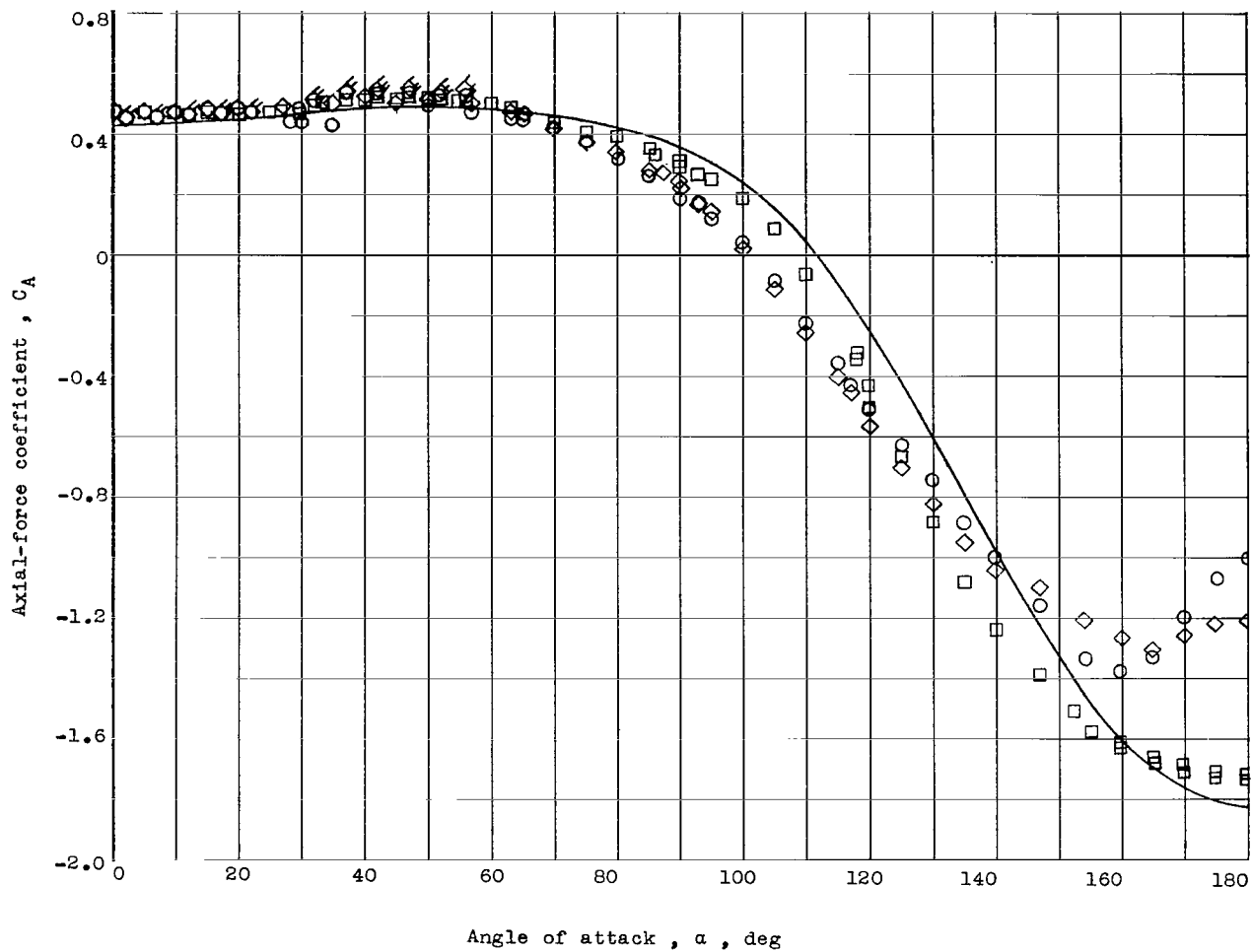


(b) Model 2.

Figure 5.- Concluded.

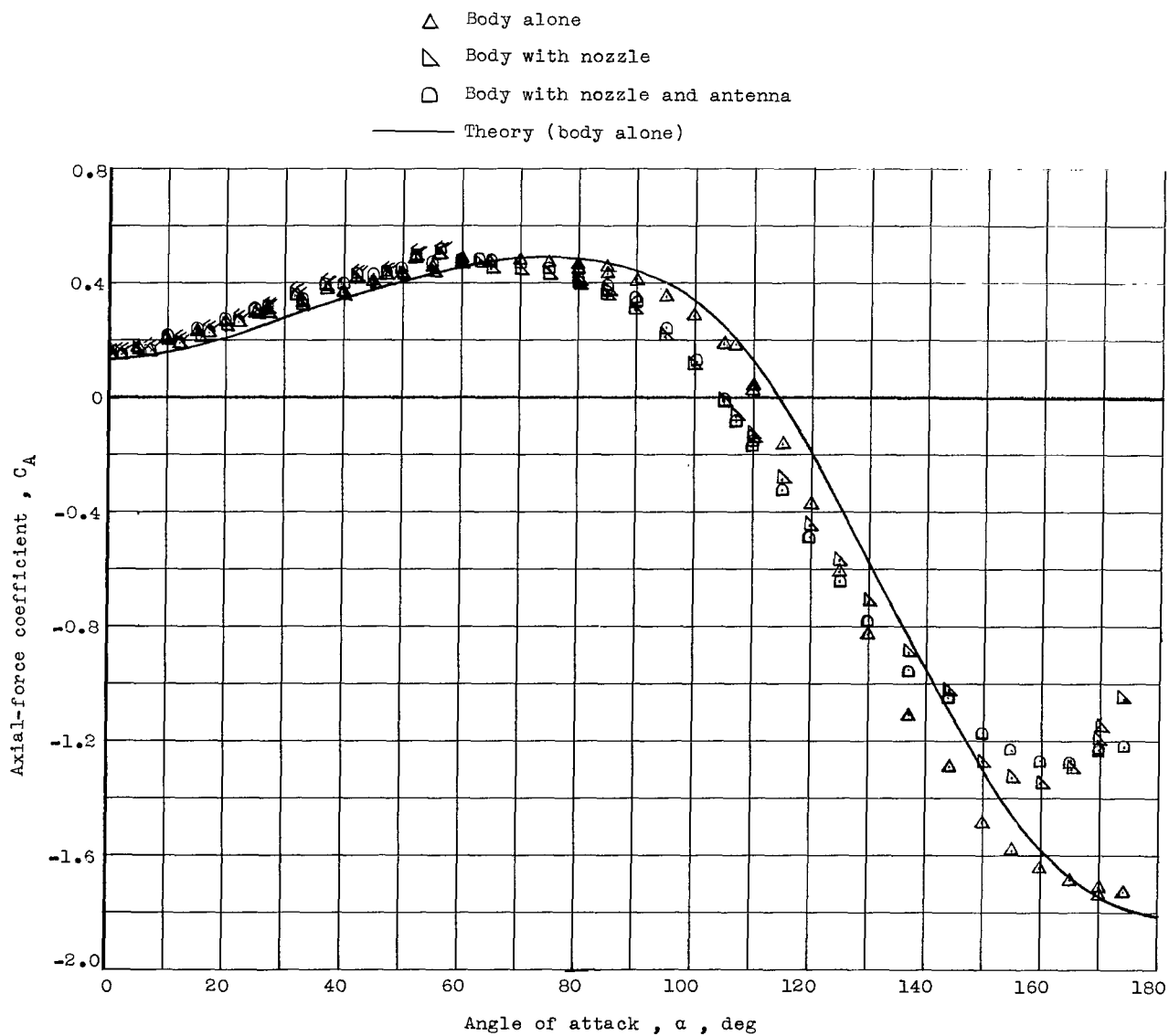
- Body alone
- Body with nozzle
- ◇ Body with nozzle and antenna
- Theory (body alone)

Flagged symbols denote helium data



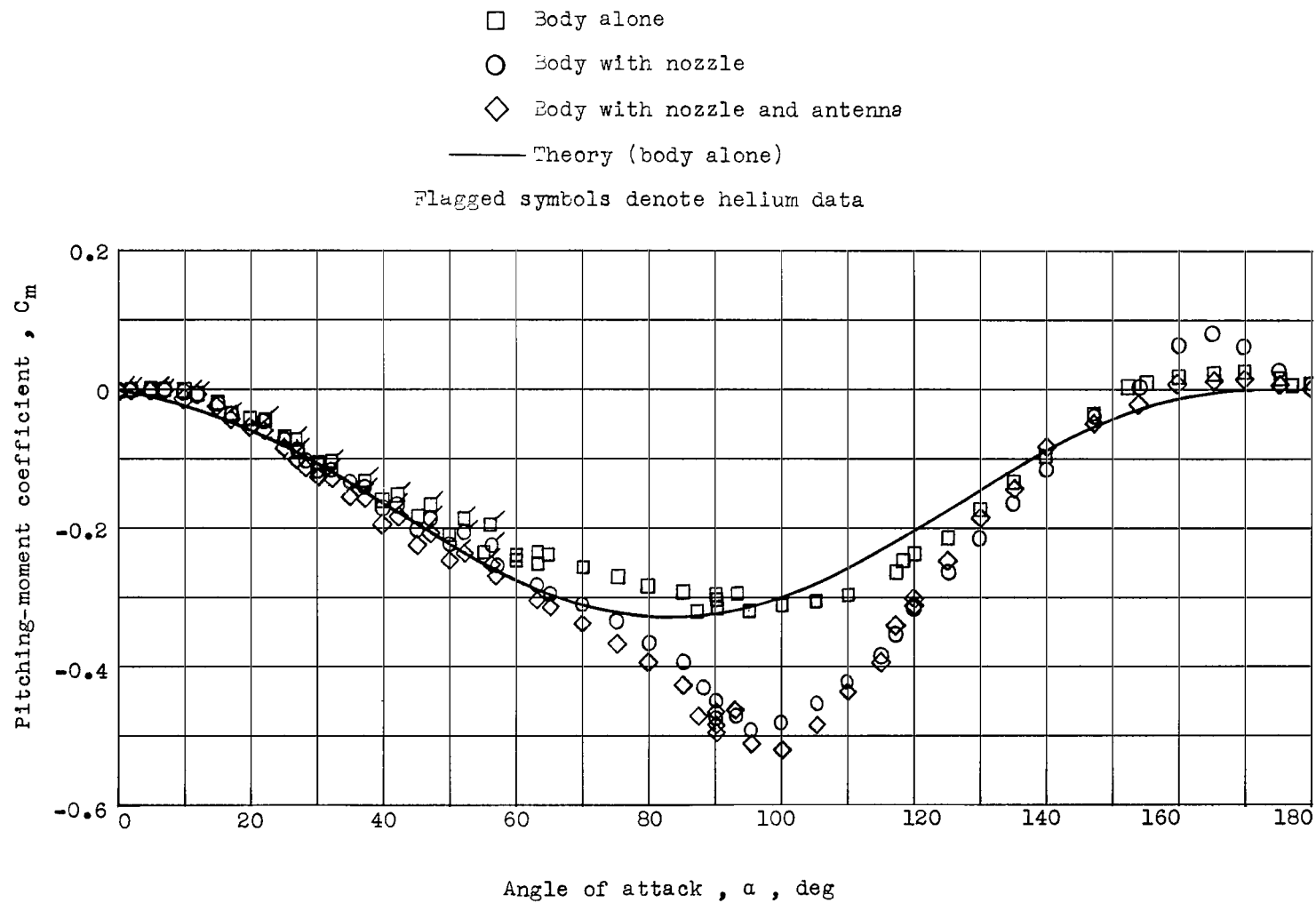
(a) Model 1.

Figure 6.- Variation of axial-force coefficient with angle of attack.



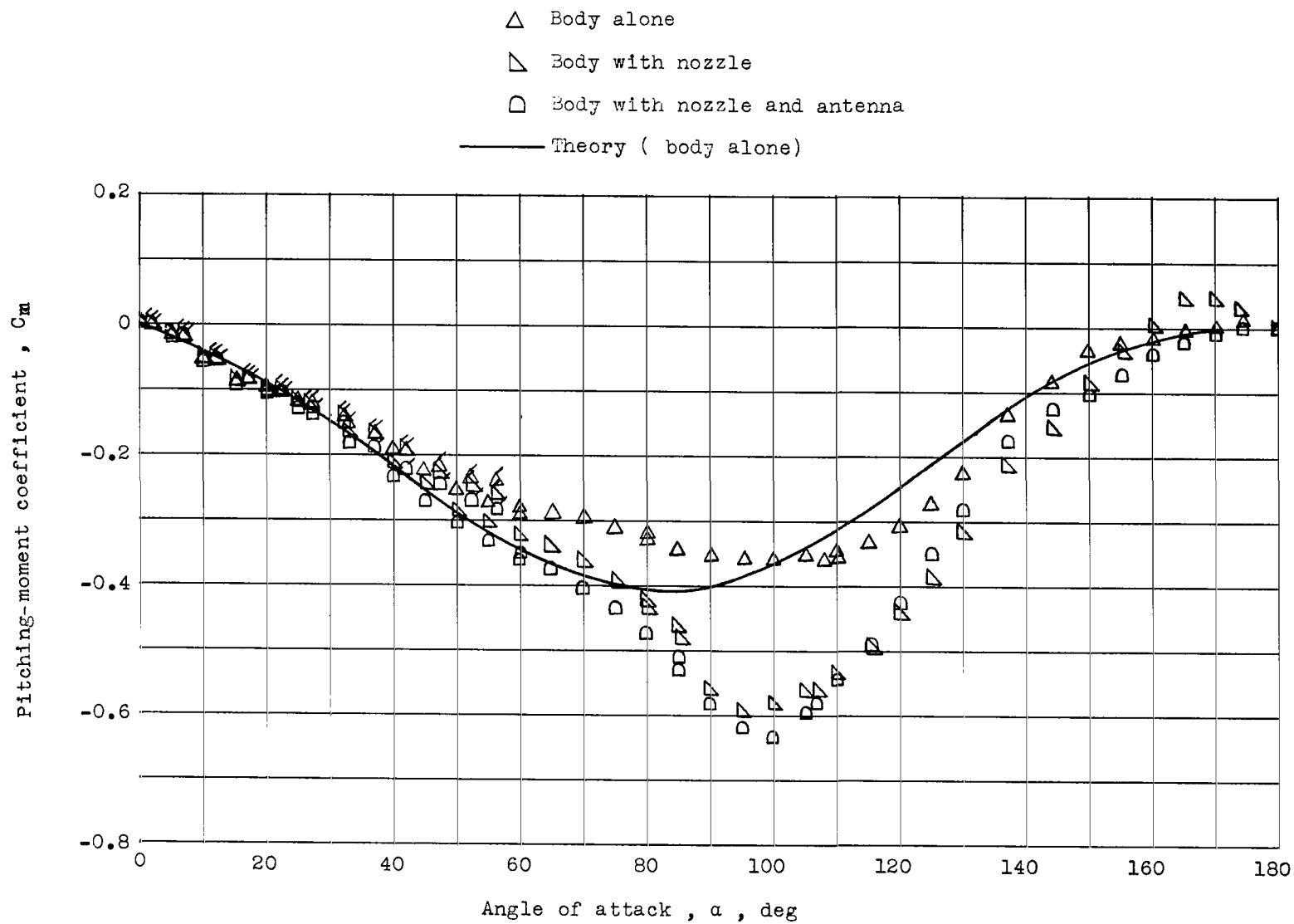
(b) Model 2.

Figure 6.- Concluded.



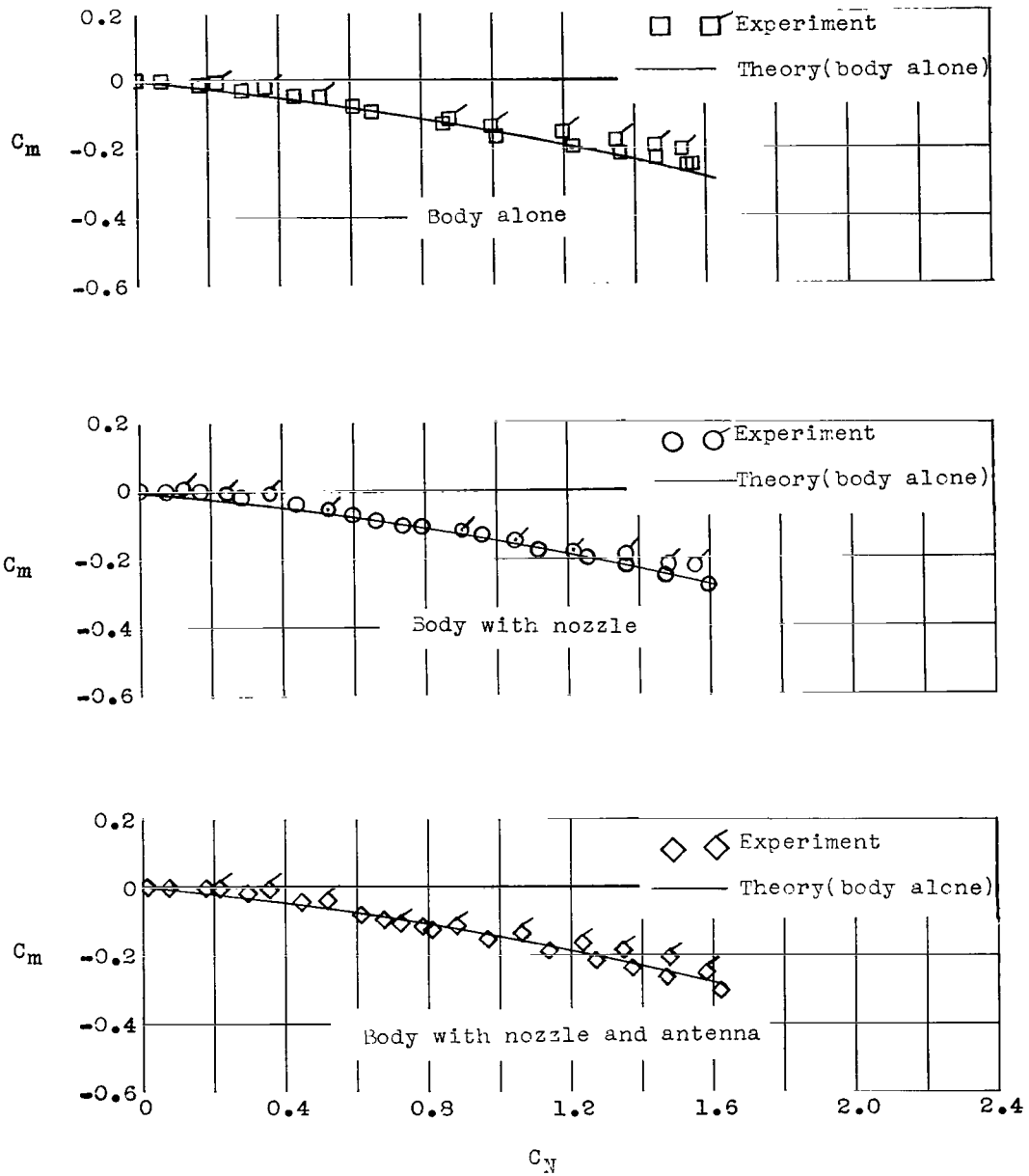
(a) Model 1.

Figure 7.- Variation of pitching-moment coefficient with angle of attack.



(b) Model 2.

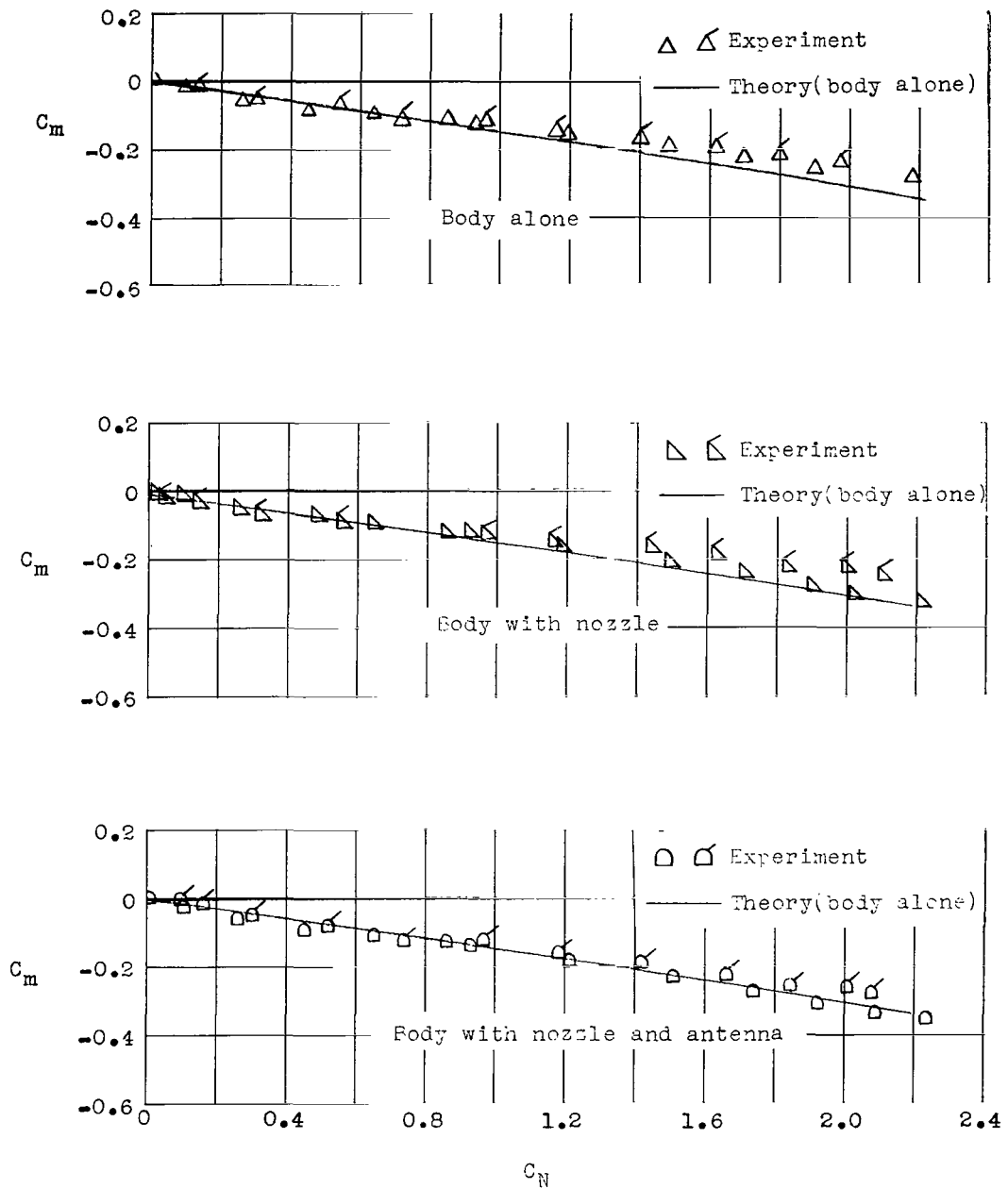
Figure 7.- Concluded.



(a) Model 1.

Figure 8.- Stability parameter  $C_m$  against  $C_N$ . Flagged symbols denote helium data.





(b) Model 2.

Figure 8.- Concluded.

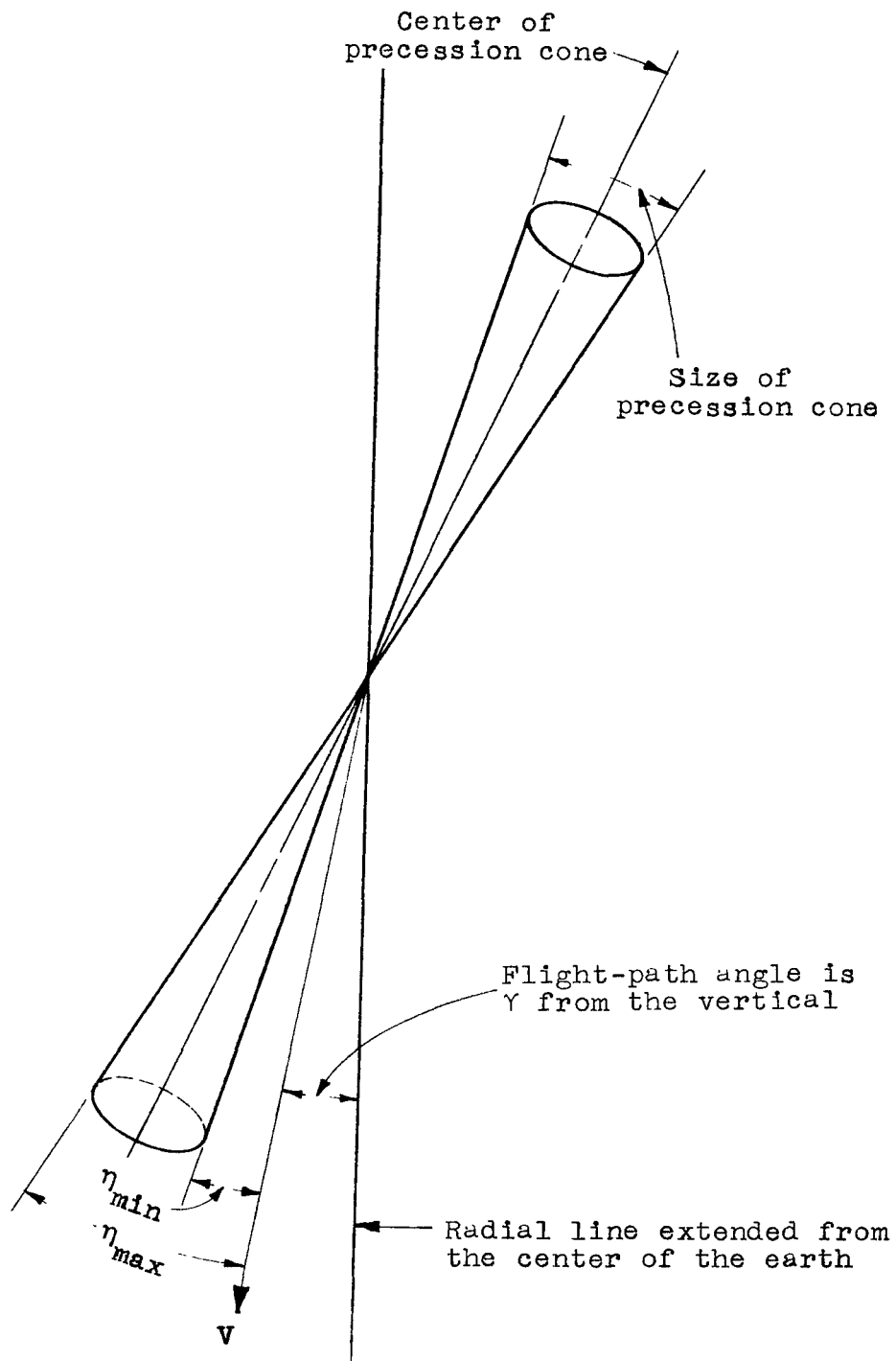


Figure 9.- Sketch of the spatial orientation of the initial precession cone without nutation and some of the nomenclature.

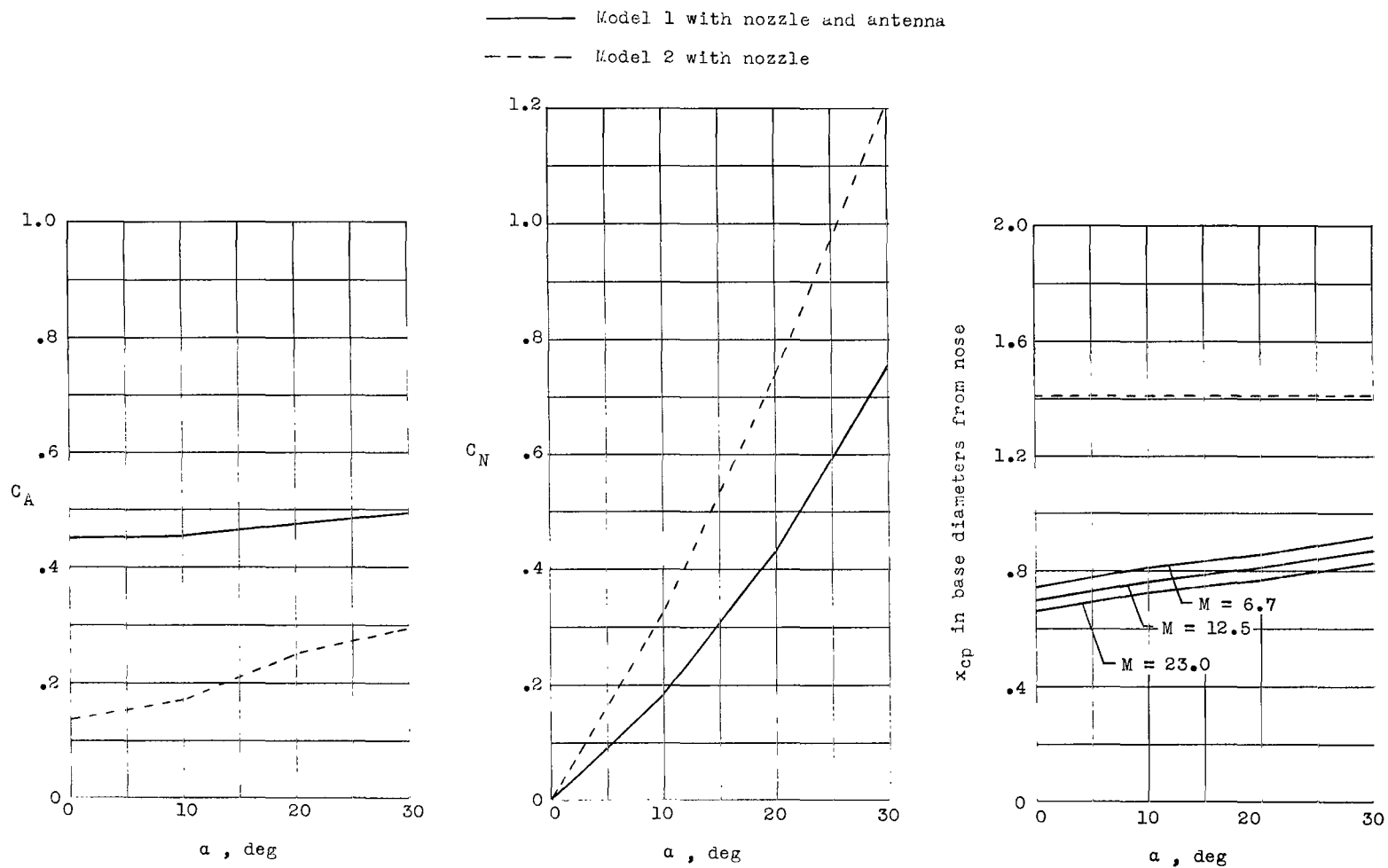
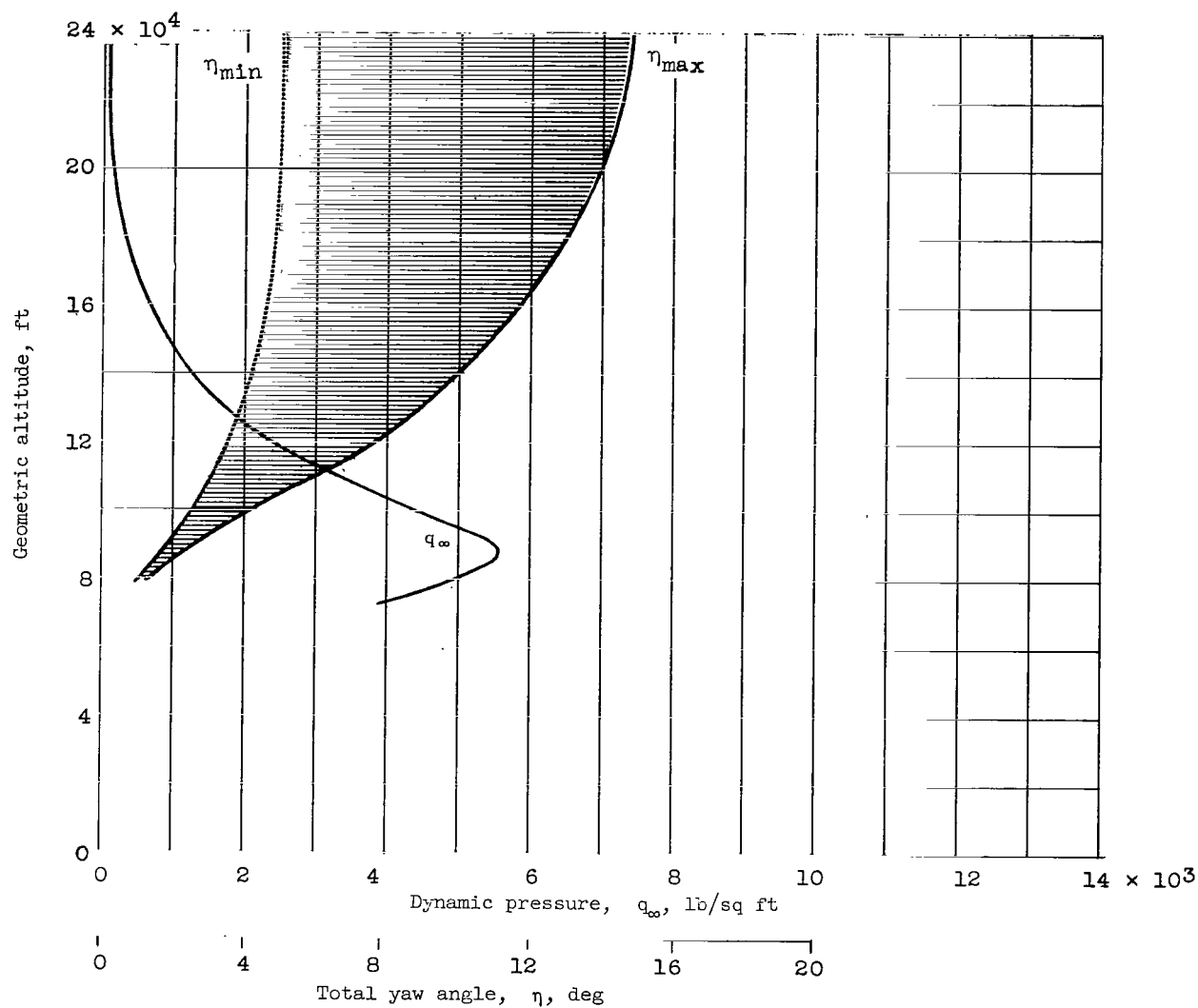
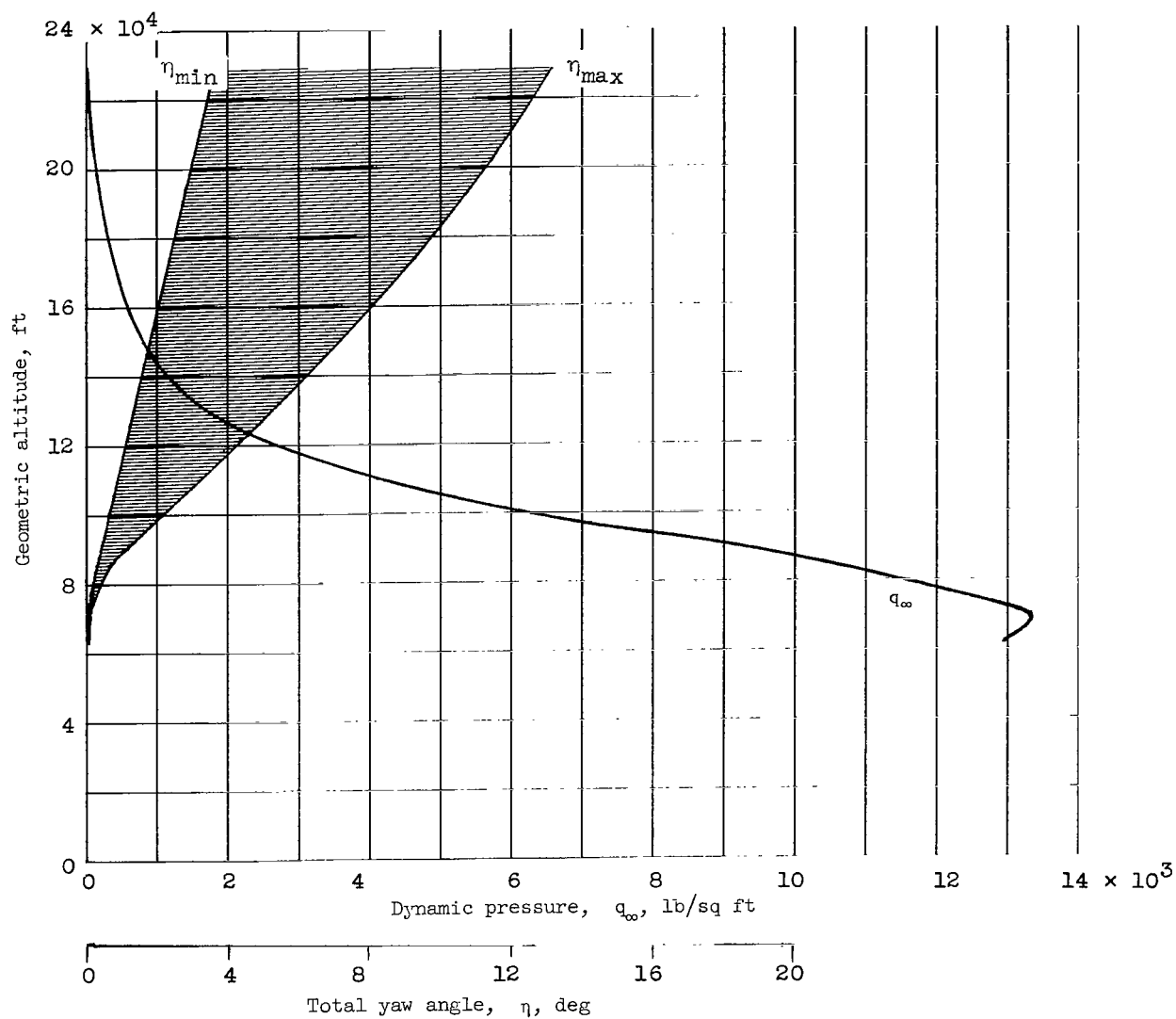


Figure 10.- Illustration of the straight-line variations made to  $C_A$ ,  $C_N$ , and center of pressure for the computer program.



(a) Model 1 with nozzle and antenna.

Figure 11.- Variation of maximum and minimum total yaw angle and dynamic pressure with altitude.



(b) Model 2 with nozzle.

Figure 11.- Concluded.

2/22/85  
07

*"The aeronautical and space activities of the United States shall be conducted so as to contribute . . . to the expansion of human knowledge of phenomena in the atmosphere and space. The Administration shall provide for the widest practicable and appropriate dissemination of information concerning its activities and the results thereof."*

—NATIONAL AERONAUTICS AND SPACE ACT OF 1958

## NASA SCIENTIFIC AND TECHNICAL PUBLICATIONS

**TECHNICAL REPORTS:** Scientific and technical information considered important, complete, and a lasting contribution to existing knowledge.

**TECHNICAL NOTES:** Information less broad in scope but nevertheless of importance as a contribution to existing knowledge.

**TECHNICAL MEMORANDUMS:** Information receiving limited distribution because of preliminary data, security classification, or other reasons.

**CONTRACTOR REPORTS:** Technical information generated in connection with a NASA contract or grant and released under NASA auspices.

**TECHNICAL TRANSLATIONS:** Information published in a foreign language considered to merit NASA distribution in English.

**TECHNICAL REPRINTS:** Information derived from NASA activities and initially published in the form of journal articles.

**SPECIAL PUBLICATIONS:** Information derived from or of value to NASA activities but not necessarily reporting the results of individual NASA-programmed scientific efforts. Publications include conference proceedings, monographs, data compilations, handbooks, sourcebooks, and special bibliographies.

*Details on the availability of these publications may be obtained from:*

SCIENTIFIC AND TECHNICAL INFORMATION DIVISION  
NATIONAL AERONAUTICS AND SPACE ADMINISTRATION

Washington, D.C. 20546